Journal of Inorganic Biochemistry 194 (2019) 180–199

Contents lists available at ScienceDirect

Journal of Inorganic Biochemistry

journal homepage: www.elsevier.com/locate/jinorgbio

Synthesis and encapsulation of V(IV,V) compounds in silica nanoparticles targeting development of antioxidant and antiradical nanomaterials

E. Halevas[a,c], C.M. Nday[a,b], D. Eleftheriadou[a], G. Jackson[b], V. Psycharis[d], C.P. Raptopoulou[d], D.G. Reid[e], K. Ypsilantis[f], G. Litsardakis[c], A. Salifoglou[a,*]

[a] Laboratory of Inorganic Chemistry and Advanced Materials, Department of Chemical Engineering, Aristotle University of Thessaloniki, Thessaloniki 54124, Greece
[b] Department of Chemistry, University of Cape Town, Rondebosch 7700, Cape Town, South Africa
[c] Laboratory of Materials for Electrotechnics, Department of Electrical and Computer Engineering, Aristotle University of Thessaloniki, Thessaloniki 54124, Greece
[d] Institute of Nanoscience and Nanotechnology, N.C.S.R. "Demokritos", Aghia Paraskevi 15310, Attiki, Greece
[e] Department of Chemistry, University of Cambridge, Lensfield Road, Cambridge CB2 1EW, UK
[f] Department of Chemistry, University of Ioannina, Ioannina 45110, Greece

ARTICLE INFO

Keywords:
Vanadium complex synthesis
Hydroxycarboxylic acid
Sol-gel encapsulation-release
Silica nanoparticles
Oxidative stress
Antioxidant-antiradical activity

ABSTRACT

The quest for effective treatments of oxidative stress has concentrated over the years on new nanomaterials with improved antioxidant and antiradical activity, thereby attracting broad research interest. In that regard, research efforts in our lab were launched to pursue such hybrid materials involving a) synthesis of silica gel matrices, b) evaluation of the suitability of atoxic matrices as potential carriers for the controlled release of V(IV)($VOSO_4$), V(V)($NaVO_3$) compounds and a newly synthesized heterometallic lithium-vanadium(IV,V) tetranuclear compound containing vanadium-bound hydroxycarboxylic 1,3-diamine-2-propanol-*N*,*N*,*N*′,*N*′-tetraacetic acid (DPOT), and c) investigation of structural and textural properties of silica nanoparticles (NPs) by different and complementary characterization techniques, inquiring into the nature of the encapsulated vanadium species and their interaction with the siloxane matrix, collectively targeting novel antioxidant and antiradical nanomaterials biotechnology. The physicochemical characterization of the vanadium-loaded SiO_2 NPs led to the formulation of optimized material configuration linked to the delivery of the encapsulated antioxidant-antiradical load. Entrapment and drug release studies showed a) the competence of hybrid nanoparticles with respect to encapsulation efficiency of the vanadium compound (concentration dependence), b) congruence with the physicochemical features determined, and c) a well-defined release profile of NP load. Antioxidant properties and the free radical scavenging capacity of the new hybrid materials (containing $VOSO_4$, $NaVO_3$, and V-DPOT) were demonstrated through a) 2-diphenyl-1-picrylhydrazyl (DPPH) free radical, and b) intracellular-extracellular reactive oxygen species (ROS) assays, through UV–Visible spectroscopy techniques, collectively showing that the hybrid silica NPs (empty-loaded) could serve as an efficient platform for nanodrug formulations counteracting oxidative stress.

1. Introduction

Vanadium is one of the trace elements essential to numerous living organisms. Complexation of that element, in various oxidations states, with bioligand substrates has been shown to carry important information for metalloprotein host structure and function. In that respect, vanadium-organoligand complexes have often been used to probe the structure and activity of many proteins, taking advantage of spectroscopic techniques [1]. Key to such chemistry is naturally-occurring ligands binding vanadium, with an outstanding analog example being the iron-binding siderophores. Siderophores are involved in iron homeostasis, with their binding to vanadium reflecting a secondary yet essential function [2]. In fact vanadate, inhibits the transport of iron-siderophore complexes [3], thereby proving the existence of vanadium interactions with iron transport systems.

Many natural metabolites, including glutathione, cysteine, ascorbic acid, nucleotides, and carbohydrates interact with vanadium, forming complexes [4–6]. Representative such examples involve interactions of vanadium with reduced glutathione or the enzyme superoxide dismutase, thus reflecting the potential of cellular vanadium to seek biomolecular targets in a redox rich biological milieu [7,8]. That chemistry, in fact, reflects the ability of that element to have a positive or

* Corresponding author.
E-mail address: salif@auth.gr (A. Salifoglou).

https://doi.org/10.1016/j.jinorgbio.2018.12.005
Received 17 March 2018; Received in revised form 14 November 2018; Accepted 2 December 2018
Available online 02 January 2019
0162-0134/ Crown Copyright © 2018 Published by Elsevier Inc. All rights reserved.

negative influence on the total antioxidant defense potential. This activity entails a host of mechanistic pathways and is dependent on the oxidation state of the metal ion, the employed dose, type and mode of ligand coordination, the presence of vitamin C, tocopherol, and others [9]. Various chronic diseases, such as inflammatory diseases, cancer, cardiovascular or metabolic diseases, are associated with an increased oxidative stress, a process characterized by an excessive formation of often simple, highly active ROS species, encompassing superoxide anions, hydrogen peroxides, or peroxynitrites [10,11]. As oxidative stress plays an important role in the development of many diseases, different yet well-defined and appropriately employed antioxidants emerge as useful agents counteracting those pathophysiological aberrations. In that sense, vanadium complexes emerge as promising oxidative stress counteracting agents [12].

Antioxidants preventing free radical reactions have, over the years, attracted intense scientific and economic interest in human health [13,14], food [15], and polymer [16] industries. Antioxidants, at low concentrations, retard or prevent molecular deterioration of cellular functions through adverse free radical reactions and radical-related oxidation [13–16], and protect the human body from ROS damage [13]. To that end, the global idea of antioxidant protection has also been extended into the polymer industry, targeting minimization of polymer oxidative degradation by addition of small amounts of antioxidants to polymers [16,17].

Major challenges linked to an antioxidant technology include: lifetime restriction, minimization of leaching and eventual volatilization of the antioxidant, control of thermal stability, and consequently the lifetime of the antioxidant [18]. In natural systems, these challenges have been successfully addressed by (a) sequestration of the antioxidant in a matrix, which can be a protein, carbohydrate or lipid, and (b) preventing undesired radical−radical couplings [19,20]. In recent research, incorporation of natural antioxidants in material-matrices, including silica nanoparticles (SiO_2 NPs), has been exploited as advanced technology to meet the aforementioned challenges [18,21].

Silica NPs are nowadays among the largest industrial nanotechnology products, finding applications in paints, microelectronics, pharmaceuticals, and cosmetics [21]. The specific NPs are also explored as nanocomposites for drug delivery [22]. Silica is considered biochemically inert [23], thereby extensively used as flowing-aid for nutraceutical and pharmaceutical products [18]. Nanosized SiO_2 particles with specific functionalities (e.g. antioxidant) could thus afford added-value hybrid nanomaterials that combine the advantages of each comprising component. Solid inorganic particles (e.g. SiO_2) offer distinct advantages over organic polymer matrices, as they are more thermally stable and chemically inert. Thus, immobilizing antioxidants encapsulated in SiO_2 NPs offer a unique opportunity to exploit the potential of antioxidant nanomaterials.

Poised to investigate the course of encapsulation and homogeneous dispersion of water-soluble drugs into sol-gel processed silica xerogels, targeting novel, well-defined hybrid organic-inorganic pharmaceutical nanomaterials, research on the interactive chemistry of vanadium (at the physiologically relevant oxidation states V(IV) and V(V)) with the hydroxycarboxylic 1,3-diamine-2-propanol-*N*,*N*,*N*′,*N*′-tetraacetic acid (DPOT) was pursued in aqueous media in the presence of lithium ions. The choice of DPOT was made on the premise that it is a multidentate metal ion chelator, capable of promoting complexation with vanadium ions and stabilizing mononuclear as well as oligonuclear assemblies [24]. To that end, we have a) synthesized and characterized a new binary heterometallic Li-V(IV,V) complex assembly bearing the multidentate organic ligand DPOT, b) synthesized acid and base-catalyzed silica gel matrices, b) compared and evaluated the suitability of these matrices as potential carrier materials for the controlled release of three well-defined V(IV), V(V), and V(IV,V) compounds, i.e. vanadyl sulfate (V(IV)) and sodium metavanadate (V(V)) serving as appropriate controls in the ensuing biological studies, and the newly synthesized V(IV,V) complex with the polyaminocarboxylate ligand DPOT (Scheme 1), c) investigated structural and textural properties of the emerging materials by different and complementary characterization techniques, in an effort to extract information on the nature of vanadium species and their interaction(s) with the siloxane matrix, and d) examined the biological profile of the emerging nanoparticles through their intracellular and extracellular free-radical and reactive oxygen species scavenging properties. The ultimate goal in this case was to target new hybrid materials linked to improved therapeutic activity, better protection against degradation, optimization in pharmacokinetics, better control of antioxidant biodistribution, and decreased cytotoxicity as a result of a slower, more constant vanadium release rate against oxidative stress and free radical activity.

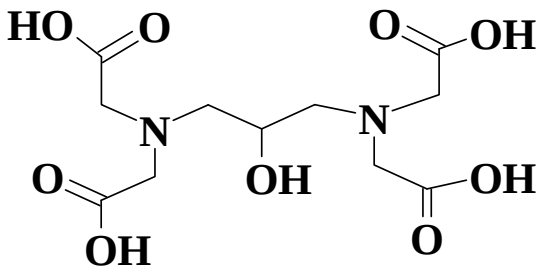

Scheme 1. Schematic representation of the ligand 1,3-diamine-2-propanol-*N*,*N*,*N*′,*N*′-tetraacetic acid (DPOT).

2. Materials and methods

2.1. Materials

All experiments were carried out under aerobic conditions. The following starting materials were purchased from commercial sources (Sigma, Fluka) and were used without further purification: Vanadium sulfate trihydrate ($VOSO_4{\cdot}3H_2O$), sodium metavanadate ($NaVO_3$), hydrochloric acid solution (HCl) (~70%), nitric acid solution (HNO_3) (70%), lithium hydroxide (LiOH), 1,3-diamine-2-propanol-*N*,*N*,*N*′,*N*′-tetraacetic acid (DPOT), tetraethyl orthosilicate (TEOS). Solvents used include: ultrapure water, ethanol (EtOH).

2.2. Physical measurements

FT-Infrared spectra were recorded on a ThermoFinnigan FT-IR 100 infrared spectrometer. A ThermoFinnigan Flash EA 1112 CHNS elemental analyser was used for the simultaneous determination of carbon, hydrogen, and nitrogen (%). The analyser operation is based on the dynamic flash combustion of the sample (at 1800 °C) followed by reduction, trapping, complete GC separation and detection of the products. The instrument is a) fully automated and controlled by PC via the Eager 300 dedicated software, and b) capable of handling solid, liquid or gaseous substances.

2.2.1. UV–Visible measurements

UV–Visible absorption measurements during the evaluation of the a) free Radical Scavenging Capacity (RSC) of vanadium-loaded SiO_2 NPs, and b) ROS assays were recorded on a Varian, Cary 500 spectrophotometer.

2.2.2. Thermal studies

A TA Instruments, model Q 600, system was used to run the TGA experiments. The instrument mass precision is 0.1 μg. A particular amount of each sample was placed in an open alumina sample pan for each experiment. A mixture of helium and high purity air (80/20 in N_2/O_2) was used at a constant flow rate of 100 mL/min, depending on the conditions required for running the experiments. During the experiments, the sample weight loss and rate of weight loss were recorded

continuously under dynamic conditions, as a function of time or temperature, in the range 45–850 °C. Prior to activating the heating routine program, the entire system was purged with the appropriate gas for 10 min, at a rate of 400 mL/min, to ensure that the desired environment had been established.

2.2.3. X-ray diffraction studies

Phase identification of the synthesized materials was accomplished through X-ray diffraction of dried powders at ambient temperature, using a Seifert XRD 3003TT powder diffractometer. The diffraction patterns of SiO_2 NPs and $NaVO_3$-SiO_2 NPs were recorded with Fe Kα radiation, while $VOSO_4$-SiO_2 NPs were measured with Cu Kα radiation, in 0.05° 2θ steps for 4 s.

2.2.4. SEM studies

The morphology and detailed structural features, down to the atomic level, were examined by scanning electron microscopy (SEM) (JEOL JSM 6300). SEM specimens were prepared by dispersing the silica powder onto a SEM holder, followed by Au coating to enhance conductivity.

2.2.5. BET and BJH measurements

The surface area of the particles and the pore size were measured by N_2 gas sorption on a surface area analyser (Autosorb-1, Quantachrome), employing the Brunauer–Emmett–Teller (BET) method. Pore volumes were estimated from adsorption branches of the isotherms using the Barrett-Joyner-Halenda (BJH) and Dubinin-Raduschevich methods.

2.2.6. Entrapment and release studies

Vanadium entrapment efficiency and release rate percentages were measured by flame atomic absorption spectrophotometry using a Perkin Elmer AAnalyst 800 instrument.

All measurements were performed immediately following sample preparation.

2.2.7. ESI-MS measurements

The Electrospray Spray Ionization mass spectrum was obtained on an Agilent Technology LC/MSD trap SL instrument and Thermo Scientific, LTQ Orbitrap XL™ high resolution system in a negative mode.

2.2.8. Solid-state NMR spectroscopy

Solid state NMR spectroscopy on the V(IV,V)-DPOT compound (**1**) and (V(IV,V)-DPOT)-loaded SiO_2 NPs was run on a Bruker Avance I NMR spectrometer with a 9.4 T superconducting magnet, operating at 100.5 MHz for ^{13}C. The samples were packed into a 4 mm zirconia rotor (Bruker). The magic angle spinning (MAS) rate was 12.5 kHz. Standard cross polarization (CP) acquisition used the following parameters: ^{1}H π/2 pulse length 2.5 μs, ^{1}H cross polarization field 70 kHz, ^{1}H-^{13}C cross polarization contact time 100 μs (particularly short on account of the paramagnetism of the samples and consequently short $T_{1\rho}$). During acquisition, SPINAL-64 decoupling at 100 kHz RF field strength was applied on ^{1}H. Repetition time was 1 s between successive acquisitions to allow relaxation. ^{13}C Chemical shifts were referenced to the methylene signal of external glycine at 43.1 ppm relative to TMS at 0 ppm.

2.3. Preparation of compound $\{[Li_4(H_2O)_8][V_4O_6(C_{11}H_{13}N_2O_9)_2]\}_n \cdot nH_2O$ (1)

To a solution of $VOSO_4 \cdot 3H_2O$ (0.22 g, 1.0 mmol) in 10 mL H_2O, DPOT (0.64 g, 2.0 mmol) was added under stirring. The resulting mixture was refluxed for 2 h under continuous stirring and then cooled to room temperature. Complete dissolution was achieved with the addition of an aqueous solution of lithium hydroxide (2.0 M) until pH 4.0. Addition of the lithium hydroxide solution continued until pH 7.5 under continuous stirring. The resulting clear reaction mixture was refluxed for an additional 2 h and then cooled to room temperature. Subsequently, the reaction flask was placed at 4 °C and ethanol was added. After three weeks, dark green needle-like crystals were obtained. The product was isolated by filtration and dried in vacuo. Yield: 0.17 g (60%). Anal. Calcd for **1**, $\{[Li_4(H_2O)_8][V_4O_6(C_{11}H_{13}N_2O_9)_2]\}_n \cdot nH_2O$ (**1**). ($C_{22}H_{44}Li_4N_4O_{33}V_4$, M_r 1124.13): C, 23.51; H, 3.95; N, 4.98. Found: C, 23.46; H, 3.92; N, 4.96. HR-ESI-MS (negative mode), calc. for $[(VO)(C_{11}H_{15}O_9N_2)]^-$ m/z = 386.0161, found m/z = 386.0157; $[Li_2(C_{11}H_{15}O_9N_2)]^-$ m/z = 333.1092, found m/z = 333.1091; and $[C_{11}H_{17}O_9N_2]^-$ m/z = 321.0929, found m/z = 321.0929.

2.4. X-ray crystal structure determination

X-ray quality crystals of **1** were grown from a water-ethanol mixture. A crystal of **1** (0.08 × 0.24 × 0.47 mm) was taken from the mother liquor and immediately cooled to −113 °C. Diffraction measurements were made on a Rigaku R-AXIS SPIDER Image Plate diffractometer using graphite monochromated Cu Kα radiation. Data collection (ω-scans) and processing (cell refinement, data reduction and numerical absorption correction) were performed using the CrystalClear program package [25]. The structure was solved by direct methods using SHELXS-97 and refined by full-matrix least-squares methods on F^2 with SHELXL-97 [26]. All hydrogen atoms were introduced through difference maps and were refined isotropically; hydrogen atoms of the coordinated and lattice water molecules were not included in the refinement. All non-hydrogen atoms were refined anisotropically. Crystallographic details for **1** are summarized in Table 1. Further experimental crystallographic details for **1**: $2\theta_{max}$ = 130°; number of reflections collected/unique/used, 34049/3468 [R (int) = 0.0602]/3468; 377 parameters refined; Δ/σ = 0.001; $(\Delta\rho)_{max}/(\Delta\rho)_{min}$ = 0.890/−0.660 e/Å^3; R/R_w (for all data), 0.0570/0.1495.

2.5. Synthesis

2.5.1. Synthesis of $VOSO_4$-loaded SiO_2 NPs

2.5 mL of TEOS was dissolved in 70 mL of H_2O. To the mixture, 20 mL of EtOH was added under continuous stirring. Subsequently, 0.80 mL of hydrochloric acid was added under continuous stirring. TEOS was left to hydrolyze for 1 h at 50 °C under continuous stirring using hydrochloric acid as a catalyst. The solution was then cooled to room temperature. Subsequently, 0.25 g of $VOSO_4 \cdot 3H_2O$ was added to the reaction mixture under continuous stirring. The resulting solution

Table 1
Crystallographic data for $\{[Li_4(H_2O)_8][V_4O_6(C_{11}H_{13}N_2O_9)_2]\}_n \cdot nH_2O$ (**1**).

Data	1
Formula	$C_{22}H_{44}Li_4N_4O_{33}V_4$
Formula weight	1124.13
Space group	*Pccn*
a (Å)	20.2257(3)
b (Å)	20.3502(3)
c (Å)	9.9334(1)
α (°)	90.0
β (°)	90.0
γ (°)	90.0
V (Å^3)	4088.56(9)
Z	4
T (°C)	−113
Radiation	Cu Kα
ρ_{calcd} (g cm^{-3})	1.826
μ (mm^{-1})	8.487
Reflections with $I > 2\sigma(I)$	3033
R^a	0.0520
$R_w{}^a$	0.1431

[a] $w = 1/[\sigma^2(F_o^2) + (\alpha P)^2 + bP]$ and $P = [\max(F_o^2,0) + 2F_c^2]/3$, $R = \Sigma(||F_o| - |F_c||)/\Sigma(|F_o|)$ and $R_w = \{\Sigma[w(F_o^2 - F_c^2)^2]/\Sigma[w(F_o^2)^2]\}^{1/2}$.

was stirred vigorously in a closed vessel at room temperature for 24 h. A blue-colored gel was obtained. The gelled system was kept for three days at room temperature before drying. The gel was fully dried in air at 110 °C in an electric oven for 12 h. The blue-colored precipitate was washed three times with ultrapure water, and dried at 90 °C for three days. The molar ratio of TEOS:EtOH:$VOSO_4{\cdot}3H_2O$:HCl:H_2O in the starting reaction solution was 0.0112:0.3425:0.00115:0.0099:3.90.

2.5.2. Synthesis of $NaVO_3$-loaded SiO_2 NPs

0.25 g of $NaVO_3$ was dissolved in 10 mL of H_2O. Complete dissolution of $NaVO_3$ was achieved after stirring at 70 °C for 5 min. Subsequently, 2.5 mL of TEOS was dissolved in 58 mL of H_2O. To the mixture, 20 mL of EtOH was added under continuous stirring. Subsequently, a solution of sodium hydroxide (0.20 mmol in 2 mL of H_2O), was added under continuous stirring. TEOS was allowed to hydrolyze for 1 h at 50 °C under continuous stirring, using sodium hydroxide as a catalyst [27]. The solution was cooled to room temperature and then the aforementioned $NaVO_3$ solution was added to the TEOS mixture under continuous stirring. The resulting solution was stirred vigorously in a closed vessel at room temperature for 24 h. A light yellow-colored gel was obtained. The gelled system was kept for three days at room temperature before drying. The gel was fully dried in air at 110 °C in an electric oven for 12 h. The yellow-colored precipitate was washed three times with ultrapure water, and dried at 90 °C for three days. The molar ratio of TEOS:EtOH:$NaVO_3$:NaOH:H_2O in the starting reaction solution was 0.0112:0.3425:0.00205:0.002:3.90.

2.5.3. Synthesis of $\{[Li_4(H_2O)_8][V_4O_6(C_{11}H_{13}N_2O_9)_2]\}_n{\cdot}nH_2O$-loaded SiO_2 NPs

TEOS (2.5 mL) was dissolved in 70 mL of H_2O. To the mixture, 20 mL of EtOH was added under continuous stirring. TEOS was allowed to hydrolyze for 1 h at 50 °C under continuous stirring, with no addition of an acidic or a basic catalyst, in order to maintain the V(IV,V) cores of the complex. The solution was cooled to room temperature and then 0.25 g of compound **1** was added to the reaction mixture under continuous stirring. The resulting solution was vigorously stirred in a closed vessel at room temperature for 24 h. A green colored gel was obtained. The gelled system was kept for three days at room temperature before drying. The gel was fully dried in air at 110 °C in an electric oven for 12 h. The green-colored precipitate was washed three times with ultrapure water, and dried at 90 °C for three days. The molar ratio of TEOS:EtOH:$\{[Li_4(H_2O)_8][V_4O_6(C_{11}H_{13}N_2O_9)_2]\}_n{\cdot}nH_2O$:$H_2O$ in the starting reaction solution was 0.0112:0.3425:0.00022:0.0099:3.90.

Pure silica (SiO_2) gel-derived glass was also synthesized by hydrolyzing TEOS under the conditions described above. A colorless precipitate was obtained in the case of the empty silica NPs. The precipitate was washed three times with ultrapure water, dried at 90 °C for three days and calcinated at 550 °C for 3 h. All three types of derived materials are shown in Scheme 2.

2.6. Determination of entrapment efficiency

The percentage of vanadium incorporated into silica NPs was determined by flame atomic absorption spectrophotometry using a Perkin Elmer AAnalyst 800 instrument. A 0.070 g dry sample was placed in a 5 mL volumetric flask and left stirring for 24 h at 37 °C in a Titertek orbital shaker, with 2 mL of Supra Pure Merck 36% HNO_3 and ultrapure water, until the sample had been completely dissolved. Appropriate dilution was applied, if necessary, and the vanadium content was determined with acetylene as fuel and nitrous oxide as the oxidant, (rich red oxidizing flame) with the spectrometer set at 318.40 nm with a 0.70 nm slit width. The 318.40 nm vanadium line is actually a triplet (318.30 nm/318.40 nm/318.50 nm). The calibration curve was linear and in the range from 20 to 200 $mg{\cdot}L^{-1}$. Characteristic concentrations of examined samples were ~90 $mg{\cdot}L^{-1}$.

The entrapment efficiency of the vanadium compound was calculated using the following equation: Entrapment Efficiency (%) = $V_i / V_t \times 100$, where V_i is the amount of vanadium compound incorporated into silica NPs and V_t is the initially added amount of the vanadium compound. Experiments were carried out in triplicates and the results were expressed as mean ± Standard deviation (SD).

2.7. In vitro vanadium release study

Drug release profiles of all types of vanadium-loaded silica NPs were performed as follows: 0.10 g of vanadium-loaded silica NP powder was ground and immersed into 50 mL of oxygenated (O_2, 100%) saline solution of the following composition (in mM): 136 NaCl, 11 glucose, 4.7 KCl, 2.4 $CaCl_2$, 1.1 $MgCl_2$, 1 $NaHCO_3$, 10 HEPES, pH 7.4) [28]. The release medium temperature was set at 37 ± 1 °C under continuous stirring at a rate of ca. 300 rpm. Aliquots of 4 mL were withdrawn with a syringe at fixed time intervals for analysis. Following removal of insoluble solid vanadium-loaded SiO_2 NPs by centrifugation (13,000 rpm, 1 min), the remaining clear solution was analyzed by inductively coupled plasma mass spectroscopy using an Agilent 7700 ICP-MS instrument. The amount of vanadium released was determined at 292.40 nm [29], with the aid of the following calibration curve:

$$C_V = 10{,}116ABS + 4{,}820 \ (R^2 = 0.9997)$$

where C_V stands for vanadium concentration in the sample ($mg{\cdot}L^{-1}$) and ABS is the absorption of the sample measured at 292.40 nm. Experiments were carried out in triplicates and the results were expressed as mean ± SD.

2.8. Determination of ROS - superoxide anion radical - scavenging activity

Superoxide anion radicals ($O_2^{\cdot -}$) are generated in vitro in a non-enzymatic phenazine methosulfate-NADH (PMS-NADH) system and determined spectrophotometrically through the nitroblue tetrazolium (NBT) reduction method. The specific ROS, created intracellularly or secreted extracellularly, following treatment of two bacterial strains *Bacillus subtilis* (BS) and *Escherichia coli* (EC) with vanadium-loaded NPs, were measured through NBT reduction, using the protocol described in the literature [30]. For this purpose, 100 μL of bacterial suspension (where OD_{600} = 1.5) in Minimal Mineral Salts (MMS) medium was incubated with the requisite vanadium compound NPs and 500 μL of 0.5 $mg{\cdot}mL^{-1}$ NBT at 37 °C. Then, 100 μL of 0.1 M HCl was added and the sample Eppendorf tubes were centrifuged at 1500*g* for 10 min. The pellets were treated with 600 μL DMSO to extract the reduced NBT. Finally, 500 μL MMS was added and formazan blue obtained from cells was measured as optical density (OD) at 575 nm (intracellular ROS), while the blue color of supernatants (extracellular ROS) was measured at the same wavelength. The amount of each type of vanadium compound and vanadium-loaded SiO_2 NPs employed for the current stage of the experiment was 0.5, 1, 2.5, 5, 15, and 25 $\mu g{\cdot}mL^{-1}$. Decreased absorbance of the incubation reaction mixture indicated increased superoxide anion radical scavenging activity [31,32]. The experiments were done in triplicates.

2.9. Radical Scavenging Capacity (RSC) assay

The RSC of the vanadium-loaded SiO_2 NPs was monitored using the standardized DPPH free radical-method [33], which offers a suitable basis for comparative evaluation of the RSC for most natural antioxidants [34,35]. Free vanadium and vanadium-loaded SiO_2 NP amounts of 10, 20, 40, 100 and 150 μg were diluted in 1 mL of methanol to make the stock suspensions. Subsequently, 100 μL of the stock suspensions in methanol and 3 mL of methanolic solution of DPPH (0.1 mM) were mixed inside 1 cm quartz cuvettes (Hellma suprasil quartz glass, 100-QS). Absorbance measurements started immediately and were recorded at 1, 2, 3, and 24 h. The decrease in absorbance at 520 nm was determined using a U-2800 Digilab Hitachi

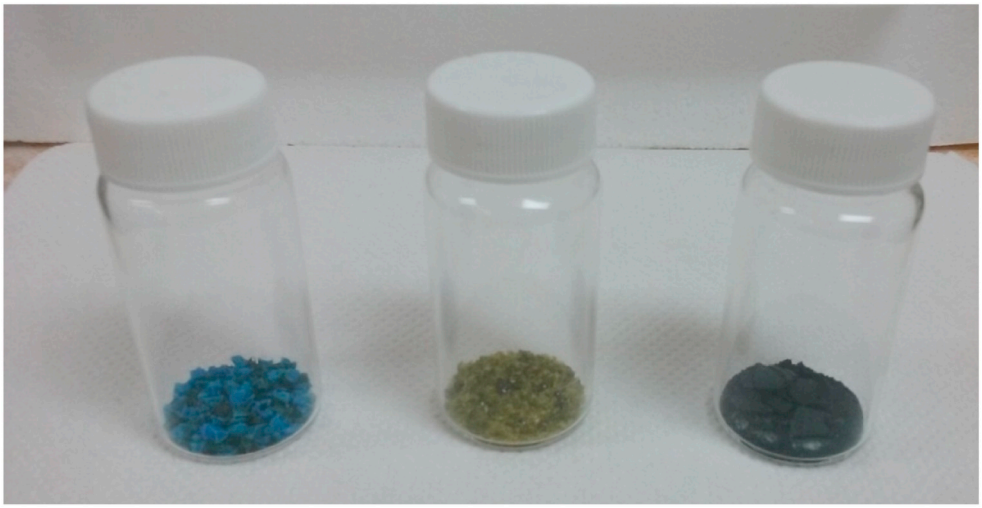

Scheme 2. From left to right: a) $VOSO_4$-loaded SiO_2 NPs, b) $NaVO_3$-loaded SiO_2 NPs, and c) $\{[Li_4(H_2O)_8][V_4O_6(C_{11}H_{13}N_2O_9)_2]\}_n{\cdot}nH_2O$-loaded SiO_2 NPs.

spectrophotometer. The samples $VOSO_4$, $NaVO_3$, V(IV,V)-DPOT, and SiO_2 were run for comparison with the results of vanadium-loaded NPs, $VOSO_4$-SiO_2 NPs, $NaVO_3$-SiO_2 NPs, and V(IV,V)-DPOT-SiO_2 NPs. With respect to $VOSO_4$ and $NaVO_3$, these vanadium compounds were employed as well-recognizable forms of vanadium species bearing oxidation states that could serve as controls for any meaningful comparisons of their individual effects. Beyond that, the specific vanadium oxidation state species are good starting materials for the synthesis of a significant number of bioinorganic compounds that have been used in biological experiments of variable nature and significance in health and disease. It is worth noting that all of the initial compounds used for vanadium antiradical and ROS determination experiments were sonicated for 15 min at 45 °C to maximize their solubility in ddH_2O prior to implementation of the antiradical and ROS experimental procedures. The RSC results emerged from a total of 24 h of incubation due to vanadium-DPPH stability, with comparable RSC profile among all free vanadium compounds and vanadium compounds loaded in silica NPs. All determinations were performed in triplicate and the results were expressed as mean ± SD.

2.10. Statistical analysis

All experiments were run in triplicate and the results were expressed as mean ± SD. The data were thus presented as average and standard error mean (SEM) values of triplicate sets of independent measurements. Mean survival rates and SEMs were calculated for each group. Absolute survival rates were calculated for each control group and one way analysis of variance (ANOVA) was performed for all pair comparisons, followed by post hoc analyses (Tukey) and Dunnet. Degrees of significance were assessed by three different rating values: *$p < 0.05$ (significant), **$p < 0.01$ (highly significant) and ***$p < 0.001$ (extremely significant) or non-significant ($p > 0.05$).

3. Results

3.1. Synthesis of $\{[Li_4(H_2O)_8][V_4O_6(C_{11}H_{13}N_2O_9)_2]\}_n{\cdot}nH_2O$ (1)

The synthetic exploration of the ternary V(IV,V)-DPOT system in this work followed carefully designed approaches. The $\{[Li_4(H_2O)_8][V_4O_6(C_{11}H_{13}N_2O_9)_2]\}_n{\cdot}nH_2O$ material was synthesized in a facile fashion from simple reagents in aqueous solutions.

In a typical reaction, $VOSO_4{\cdot}3H_2O$ reacted with DPOT (molar ratio 1:2) in the presence of lithium hydroxide at pH 7.5. The overall stoichiometric reaction leading to **1** is shown schematically below:

$$8n\ VOSO_4{\cdot}3H_2O + 4n\ C_{11}H_{18}N_2O_9 + 24n\ LiOH + n\ O_2 \xrightarrow[pH\ 7.5]{H_2O} 2\ \{[Li_4(H_2O)_8][V_4O_6(C_{11}H_{13}N_2O_9)_2]\}_n{\cdot}nH_2O + 8n\ Li_2SO_4 + 28n\ H_2O$$

Ethanol was added as a precipitating solvent to the reaction mixture. A dark green crystalline material emerged, the analytical composition of which was consistent with the formulation in **1** (vide supra). Positive identification of the crystalline product was achieved by elemental analysis, FT-IR spectroscopic methods and X-ray crystallographic determination for isolated single crystals from **1**. The compound is stable in the crystalline form, in the air, for fairly long periods of time, and is readily dissolved in water and DMSO, slightly insoluble in alcohols (CH_3OH, i-PrOH), and insoluble in acetone, acetonitrile and dichloromethane at room temperature.

3.2. Synthesis of gels

The sol–gel process involves a transition of a system from a sol, a relatively low viscous liquid, into a solid gel phase following condensation and ensuing cross-linking of the colloidal particles detectable by a sharp increase of viscosity [36]. As a precursor for the sol–gel reaction, a typical metal alkoxide, such as tetraethoxysilane (TEOS), is used. At first, the alkoxide is easily hydrolyzed by water, catalyzed by an acid or a base.

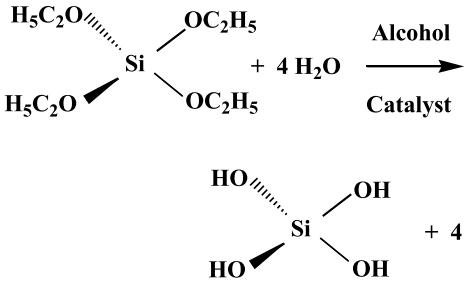

(1)

The emerging hydrated silica tetrahedra interact further, undergoing a condensation reaction and giving rise to moieties such as those shown below:

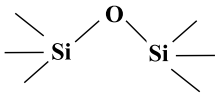

In the ensuing polycondensation process, additional silanols get linked (Scheme 3). The products of condensation are alcohol and water.

To the emerging silica sols, vanadium V(IV), V(V), and V(IV,V)

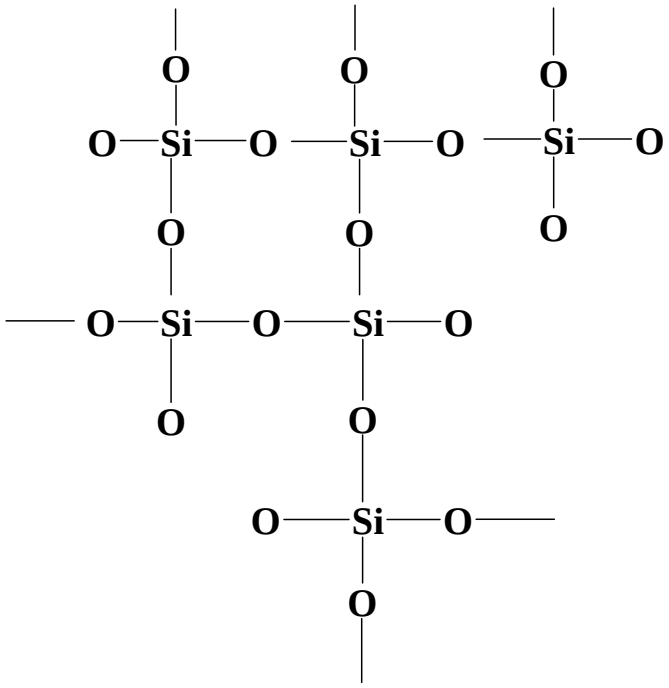

Scheme 3. Schematic illustration of the resulting silica network during the polycondensation process.

compounds were added to the corresponding preparations. The V(IV,V)-DPOT-loaded SiO_2 NP is shown in Scheme 4.

3.3. Description of X-ray crystallographic structures

The X-ray crystal structure of **1** reveals a discrete solid state lattice. The molecular structure of **1** is given in Fig. 1; selected bond distances and angles are listed in Table 2. The structure of **1** consists of tetranuclear anions $[V_4O_6(C_{11}H_{13}N_2O_9)_2]^{4-}$ residing on an inversion center, lithium Li^+ cations, and coordinated and lattice water molecules. The structure of the anion consists of two pairs of centrosymmetrically related vanadium ions, V(1) and V(2), which are bridged through the deprotonated alkoxido oxygen atom O(5) of the $DPOT^{5-}$ ligand (Fig. 1A). Atom V(1) is bound to the carboxylato oxygens O(1) and O(3), the alkoxido oxygen O(5) and the nitrogen atom N(1) of the $DPOT^{5-}$ ligand, and also to the doubly-bonded oxygens O(10) and O(12). Atom V(2) exhibits the same type of coordination as V(1) and is bound to the carboxylato oxygens O(6) and O(8), the alkoxido oxygen O(5) and the nitrogen atom N(2) of the $DPOT^{5-}$ ligand, and also to the doubly-bonded oxygen atoms O(11) and O(12)'. Both V(1) and V(2) exhibit distorted octahedral coordination geometry. The doubly bonded oxygen atoms O(12) and O(12)' bridge atoms V(1) and V(2), with their centrosymmetric counterparts V(2)' and V(1)', respectively, thus forming the tetranuclear anion. The remaining carboxylato oxygens of the DPOT ligand, O(2)/O(4)/O(7)/O(9), are bound to the Li^+ ions. Therefore, each DPOT ligand is fully deprotonated in its penta-anionic form and serves as a hexadentate ligand bridging four Li and two V ions. Li(1) is bound to two water molecules, O(1w) and O(2w), and to

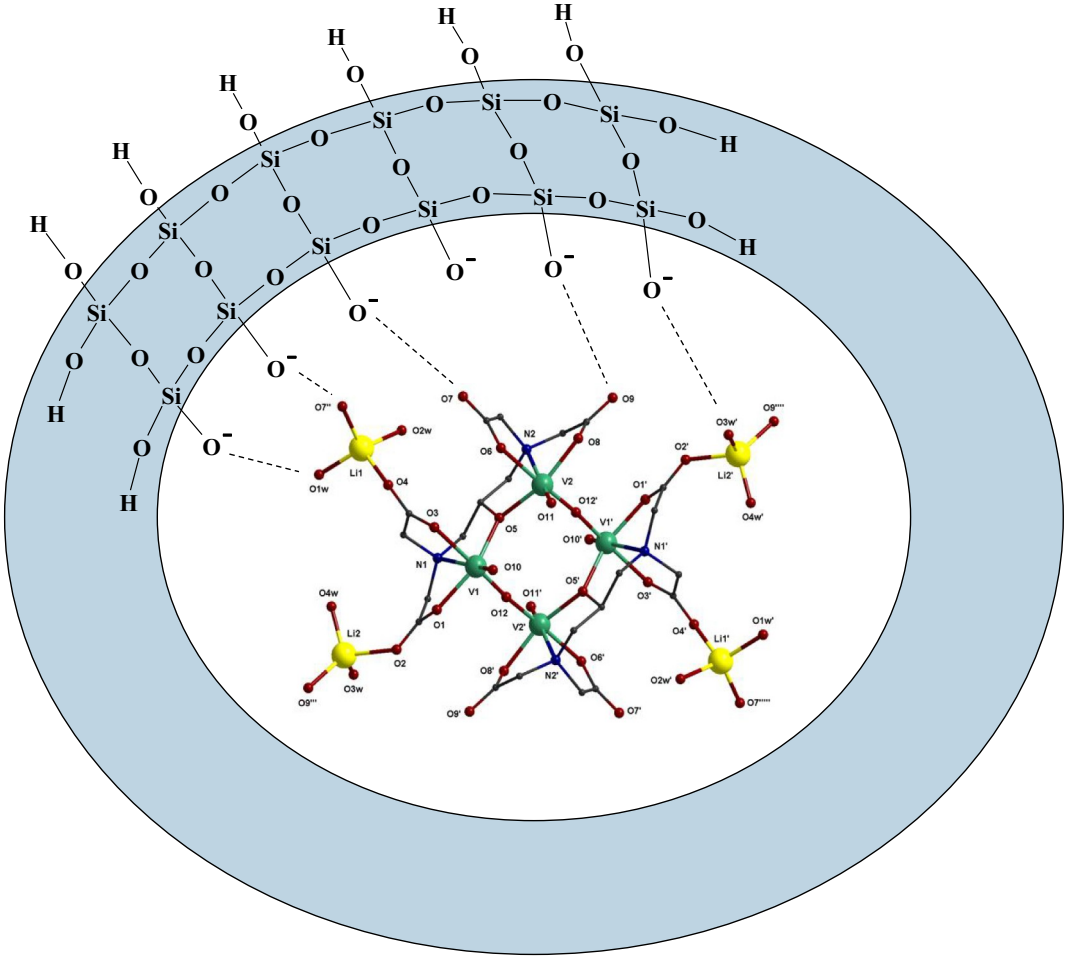

Scheme 4. Schematic illustration of the encapsulated V(IV,V)-DPOT species into the silica matrix.

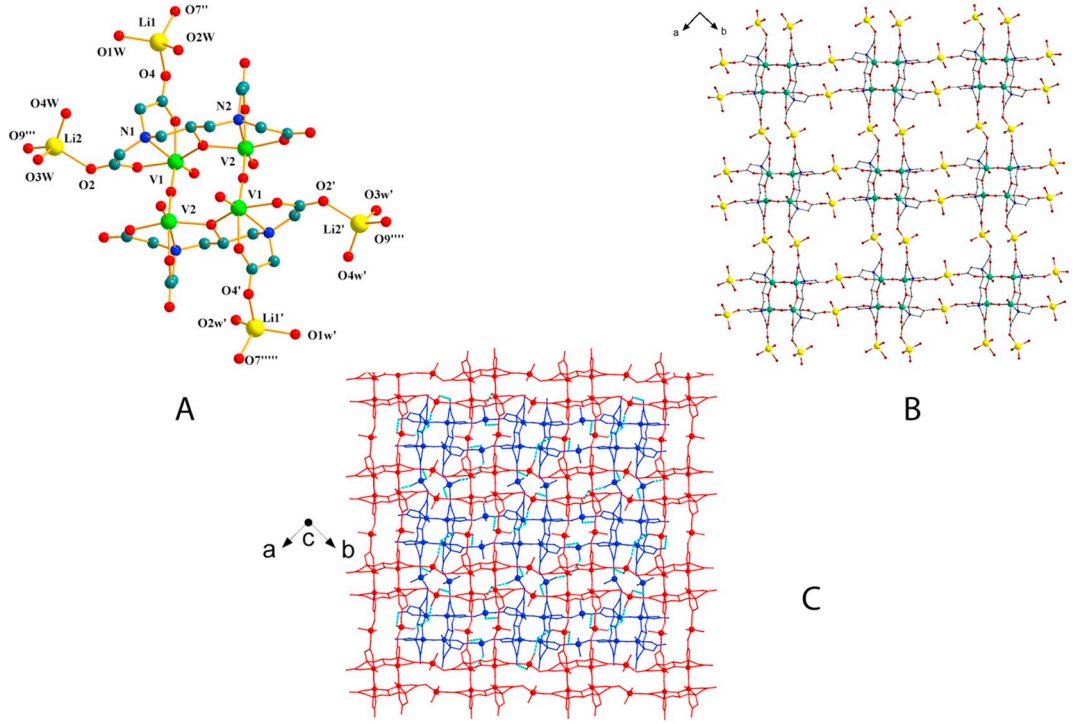

Fig. 1. A. The tetranuclear repeating unit in the structure of **1**. Hydrogen atoms are omitted for clarity. Primed atoms are generated by symmetry: (') 2 − x, 1 − y, 1 − z; (") 2.5 − x, 0.5 − y, z; ("') −0.5 + x, −0.5 + y, 1 − z; ("") 2.5 − x, 1.5 − y, z; ("") −0.5 + x, 0.5 + y, 1 − z.
B. A small part of the 2D network structure of **1** extending parallel to the crystallographic *ab* plane. Color code: V, green; Li, yellow; O, red; N, blue; C, grey.
C. Two successive layers stacked along the c axis. With blue and red colors are indicated the bottom and top layers. Thick dashed cyan lines represent possible hydrogen bonds developed between these layers. (For interpretation of the references to color in this figure legend, the reader is referred to the web version of this article.)

Table 2
Selected bond distances (Å) and angles (°) for $\{[Li_4(H_2O)_8][V_4O_6(C_{11}H_{13}N_2O_9)_2]\}_n \cdot nH_2O$ (**1**).

Distances			
V(1)-O(10)	1.601(3)	V(2)-O(11)	1.607(3)
V(1)-O(12)	1.771(2)	V(2)-O(12)'	1.844(2)
V(1)-O(5)	1.996(2)	V(2)-O(8)	2.009(2)
V(1)-O(1)	2.010(2)	V(2)-O(5)	2.025(2)
V(1)-O(3)	2.074(2)	V(2)-O(6)	2.035(2)
V(1)-N(1)	2.277(3)	V(2)-N(2)	2.273(3)

Angles			
O(10)-V(1)-O(12)	103.9(1)	O(11)-V(2)-O(12)'	102.4(1)
O(10)-V(1)-O(5)	105.7(1)	O(11)-V(2)-O(8)	100.6(1)
O(12)-V(1)-O(5)	90.6(1)	O(12)'-V(2)-O(8)	89.1(1)
O(10)-V(1)-O(1)	98.2(1)	O(11)-V(2)-O(5)	105.5(1)
O(12)-V(1)-O(1)	91.6(1)	O(12)'-V(2)-O(5)	89.4(1)
O(5)-V(1)-O(1)	154.7(1)	O(8)-V(2)-O(5)	153.5(1)
O(10)-V(1)-O(3)	91.2(1)	O(11)-V(2)-O(6)	93.7(1)
O(12)-V(1)-O(3)	164.8(1)	O(12)'-V(2)-O(6)	163.9(1)
O(5)-V(1)-O(3)	83.8(1)	O(8)-V(2)-O(6)	88.9(1)
O(1)-V(1)-O(3)	87.7(1)	O(5)-V(2)-O(6)	85.4(1)
O(10)-V(1)-N(1)	165.0(1)	O(11)-V(2)-N(2)	169.5(1)
O(12)-V(1)-N(1)	89.6(1)	O(12)'-V(2)-N(2)	87.1(1)
O(5)-V(1)-N(1)	80.1(1)	O(8)-V(2)-N(2)	74.6(1)
O(1)-V(1)-N(1)	74.7(1)	O(5)-V(2)-N(2)	78.9(1)
O(3)-V(1)-N(1)	75.6(1)	O(6)-V(2)-N(2)	77.0(1)

Symmetry operation: (') 2 − x, 1 − y, 1 − z.

the carboxylato oxygens O(4) and O(7)" belonging to two neighboring DPOT ligands. Li(2) is also bound to two water molecules, O(3w) and O (4w), and to the carboxylato oxygens O(2) and O(9)"' from two neighboring DPOT ligands. The coordination geometry around the Li^+ ions is distorted tetrahedral.

The V=O, V−$O_{carboxylato}$ and V−N bond distances are 1.601(3)–1.607(3), 1.996(2)–2.074(2), and 2.273(3)–2.777(3) Å, respectively. The bridging doubly bonded oxygen atoms exhibit longer bonding distances V(1)-O(12) = 1.771(2) and V(2)-O(12)' = 1.884 Å, respectively, as expected. The Li-O_{aqua} and Li-$O_{carboxylato}$ bond distances are in the range 1.908–1.988 and 1.888–2.040 Å, respectively.

The tetranuclear anions $[V_4O_6(C_{11}H_{13}N_2O_9)_2]^{4-}$ are linked through the Li^+ ions via coordination of the carboxylato oxygen atoms of $DPOT^{5-}$ described above and form a 2D hybrid network, which extends parallel to the crystallographic *ab* plane (Fig. 1B).

Although the hydrogen atoms of coordinated water molecules to Li^+ cations have not been located, the O(1w)···O10*, O(2w)···O4*, O (3w)···O9**, O(4w)···O10* distances possess values, 2.959, 2.717, 2.758 and 2.937 Å, respectively, which are well below the sum of van der Waals radii, indicating possible strong hydrogen bonds among these pairs of atoms [symmetry code: (*): x, 0.5 − y, 0.5 + z; (**): 2 − x, −0.5 + y, 1.5 − z]. All these bonds develop between atoms belonging to neighboring hybrid layers stacked along the c axis (Fig. 1C) and have been described previously. The lattice water molecule, O5w, is linked through hydrogen bonds to the hybrid layers [O(5w)-O11(2.5 − x, y, 0.5 + z) = 2.656 Å; O(5w)-O(4w) (0.5 + x, 0.5 + y, 1 − z) = 2.73 Å].

3.4. FT-IR spectroscopy

FT-IR spectra of the dried empty, $VOSO_4$ and $NaVO_3$-loaded gels are shown in Fig. 2A. The narrow absorption band at 1133 cm^{-1} for $VOSO_4$-SiO_2 NPs confirms the presence of sulfate ion as a monodentate inner-sphere complex in the network of the dried gel [37]. The weak band at 948 cm^{-1} for empty SiO_2 NPs is related to the vibration of Si−O−H groups [38]. The same band at 986 cm^{-1} for $VOSO_4$-SiO_2 NPs and 953 cm^{-1} for $NaVO_3$-SiO_2 NPs, respectively, is also correlated to the asymmetric stretching mode of SiO_4 tetrahedrons connected to

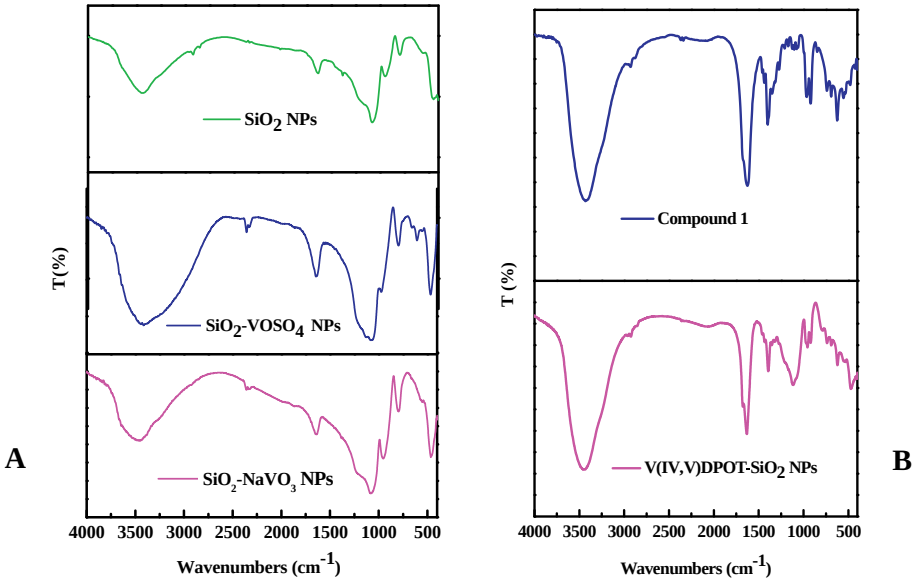

Fig. 2. A. FT-IR spectra of SiO_2 NPs, $VOSO_4$-SiO_2 NPs, and $NaVO_3$-SiO_2 NPs. **B.** FT-IR spectra of **1**, and (V(IV,V)-DPOT)-SiO_2 NPs.

V-ions. This band was also reported, in the literature, at 960 cm^{-1} and assigned to V-silicalites [39], and at about 950 cm^{-1} for vanadia-silica xerogels [40]. In other research reports, this band was assigned to a Si—O—V stretching mode. It is also suggested that both Si—O—V and V—O—V bridges can contribute to this band [41]. In general, the Si—O—V stretching bands cannot be easily detected due to possible overlapping with the silanol groups of SiO_2 [42]. Another common feature of the FT-IR spectra of all dried gels is the envelope in the 1000–1300 cm^{-1} region. It reflects the typical absorption bands of the siloxane network, which appears at 1081 cm^{-1} for empty SiO_2 NPs, 1080 cm^{-1} for $VOSO_4$-SiO_2 NPs, and 1082 cm^{-1} for $NaVO_3$-SiO_2 NPs, respectively [43–45]. Absorption bands for Si—O—Si bending vibrations are seen at about 450 cm^{-1} for empty SiO_2 NPs, 467 cm^{-1} for $VOSO_4$-SiO_2 NPs, and 464 cm^{-1} for $NaVO_3$-SiO_2 NPs, respectively. Absorption bands for Si—O—Si symmetric stretching vibrations are seen at 795 cm^{-1} for empty silica, 797 cm^{-1} for $VOSO_4$-SiO_2 NPs, and 796 cm^{-1} for $NaVO_3$-SiO_2 NPs, respectively. Absorption bands at 1637 cm^{-1} for empty SiO_2 NPs, 1645 cm^{-1} for $VOSO_4$-SiO_2 NPs, and 1639 cm^{-1} for $NaVO_3$-SiO_2 NPs, respectively, are assigned to the deformation modes of O—H bonds and the molecularly adsorbed water [46]. They are also seen as a broad absorption band in the 2750–3750 cm^{-1} range. The maximum of this band occurs at about 3444 cm^{-1} for empty SiO_2 NPs, 3415 cm^{-1} for $VOSO_4$-SiO_2 NPs, and 3457 cm^{-1} for $NaVO_3$-SiO_2 NPs, respectively, indicating the presence of hydroxyl groups involved in hydrogen-bonding of moderate strength [47].

FT-IR spectra of **1** and V(IV,V)-DPOT-loaded gels are shown in Fig. 2B. The FT-IR spectrum of **1** was recorded in KBr and reflected the presence of vibrationally active carboxylate groups. The Infrared spectrum of **1** shows antisymmetric stretching vibrations $\nu_{as}(COO^-)$ for the carboxylate carbonyls at 1625 cm^{-1}. Symmetric vibrations $\nu_s(COO^-)$ for the same groups appeared around 1401 cm^{-1}. All of the observed carbonyl vibrations were shifted to lower frequency values in comparison to the corresponding vibrations in free DPOT, suggesting changes in the vibrational status of DPOT upon coordination to vanadium. The latter indication was attested to by the X-ray crystal structures of **1**. The characteristic $\nu(V{=}O)$ stretch appears as a medium-strong band with two peaks at 966 cm^{-1} and 920 cm^{-1}, indicating the existence of V(IV) and V(V) cores [48,49]. The described tentative assignments are consistent with infrared frequencies previously attributed to carboxylate-containing ligands bound to different metal ions [50].

Absorption bands for Si—O—Si bending and symmetric stretching vibrations for V(IV,V)-DPOT-SiO_2 NPs are observed at about 471 cm^{-1} and 798 cm^{-1}, respectively. Absorption bands at 1632 cm^{-1} and around 1401 cm^{-1} are assigned to antisymmetric and symmetric stretching vibrations for the carboxylate carbonyls of the encapsulated complex. Absorption bands of O—H bonds are observed at 3448 cm^{-1}. The shoulder at about 956 cm^{-1} can be related to the stretching vibration of Si—O^- bonds.

3.5. Solid-state NMR spectroscopy

The ^{13}C CP-MAS-NMR spectrum of **1** (Fig. 3A) was consistent with the coordination mode of the $DPOT^{5-}$ ligand bound to V(IV) and V(V) ions. Specifically, the spectrum of **1** exhibits broad resonances in the range 46.0–74.0 ppm, attributed to the methylene carbons of the DPOT ligand and resonances in the range 178.0–193.0 ppm for the carboxylato carbons of the DPOT ligand bound into the V(IV) and V(V) coordination spheres [51–53]. These observations are consistent with the structure of **1** revealed by X-ray crystallography. In the case of the ^{13}C CP-MAS-NMR spectrum of V(IV,V)-DPOT-SiO_2 NPs (Fig. 3B), encapsulation in the silica matrix causes small changes in the spectrum of **1**, which may reflect interactions between the title compound and the encapsulating material (SiO_2). More detailed structural analysis is not possible at this point. The spectrum of V(IV,V)-DPOT-SiO_2 NPs exhibits broad resonances in the range 34.0–74.0 ppm, attributed to the methylene carbons of the $[DPOT]^{5-}$ ligand and resonances in the range 167.0–185.0 ppm for the carboxylato carbons of the $[DPOT]^{5-}$ ligand bound into the V(IV) and V(V) coordination spheres.

The broadness of the signals in both samples is probably attributable to the paramagnetic nature of the complexes, which shortens T_2 with concomitant increase in the linewidth. Indeed the carboxylate signals expected at about 180 ppm seem to be broadened beyond detection. The degree of signal broadening is dependent on a number of factors, including the distance of specific atoms from nearby paramagnetic centers, the number of these centers, and the segmental and overall motional properties of the complex.

3.6. TGA analyses

TGA curves of the as-prepared products are shown in Fig. 4A–C. The thermal decomposition of the as-prepared products was studied by TGA under an atmosphere of oxygen (Fig. 4A). Compound **1** is thermally stable up to 51 °C. From that point on, a fairly broad heat process points

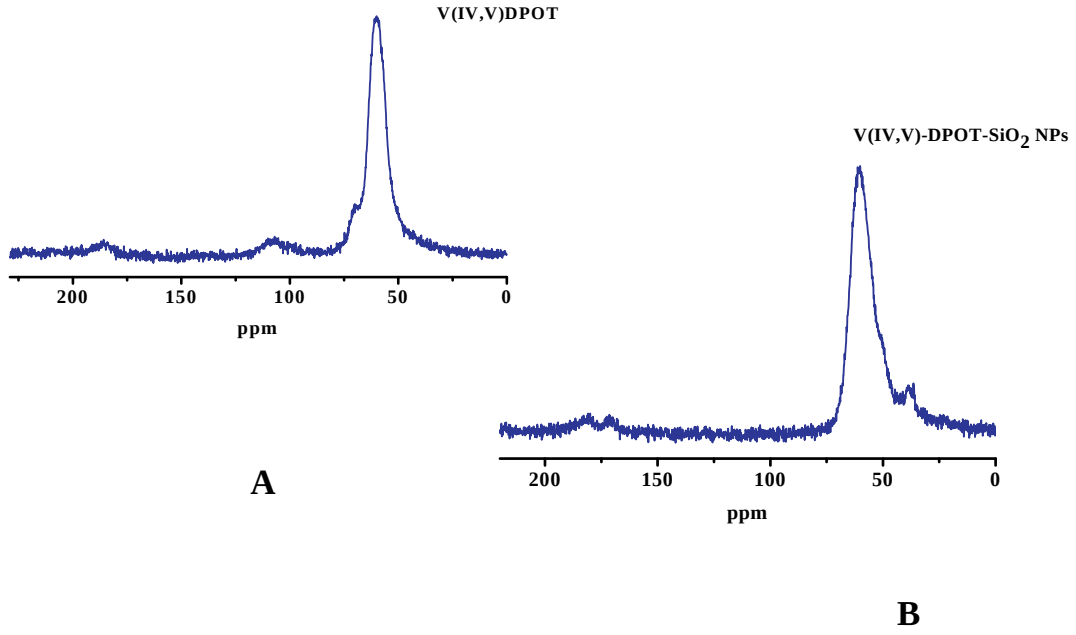

Fig. 3. A. ^{13}C-CPMAS NMR spectrum of **1**. **B.** ^{13}C-CPMAS NMR spectrum of (V(IV,V)-DPOT)-SiO_2 NPs.

to the dehydration of **1**, with release of moisture and lattice water molecules between 51 °C and 323 °C. In the range from 323 °C to 540 °C, there is further weight loss, in line with the decomposition of the organic structure of the molecule. No clear plateaus are reached in these stages, suggesting that the arising products may be unstable and decompose further (Fig. 4A). A plateau in the decomposition of **1** is reached at 540 °C, with no further loss up to 850 °C, in line with the thesis that the product at that temperature and beyond (540 °C) is $LiVO_3$. The total weight loss of ~59.3% is in good agreement with the theoretical value ~60.6% expected for the following equation:

$$\{[Li_4(H_2O)_8][V_4O_6(C_{11}H_{13}N_2O_9)_2]\}_n{\cdot}nH_2O + 22.5n\ O_2 \rightarrow 4n\ LiVO_3 + 2n\ N_2 + 22n\ CO_2 + 22n\ H_2O$$

Examination of the residue by SEM and XRD showed the presence of

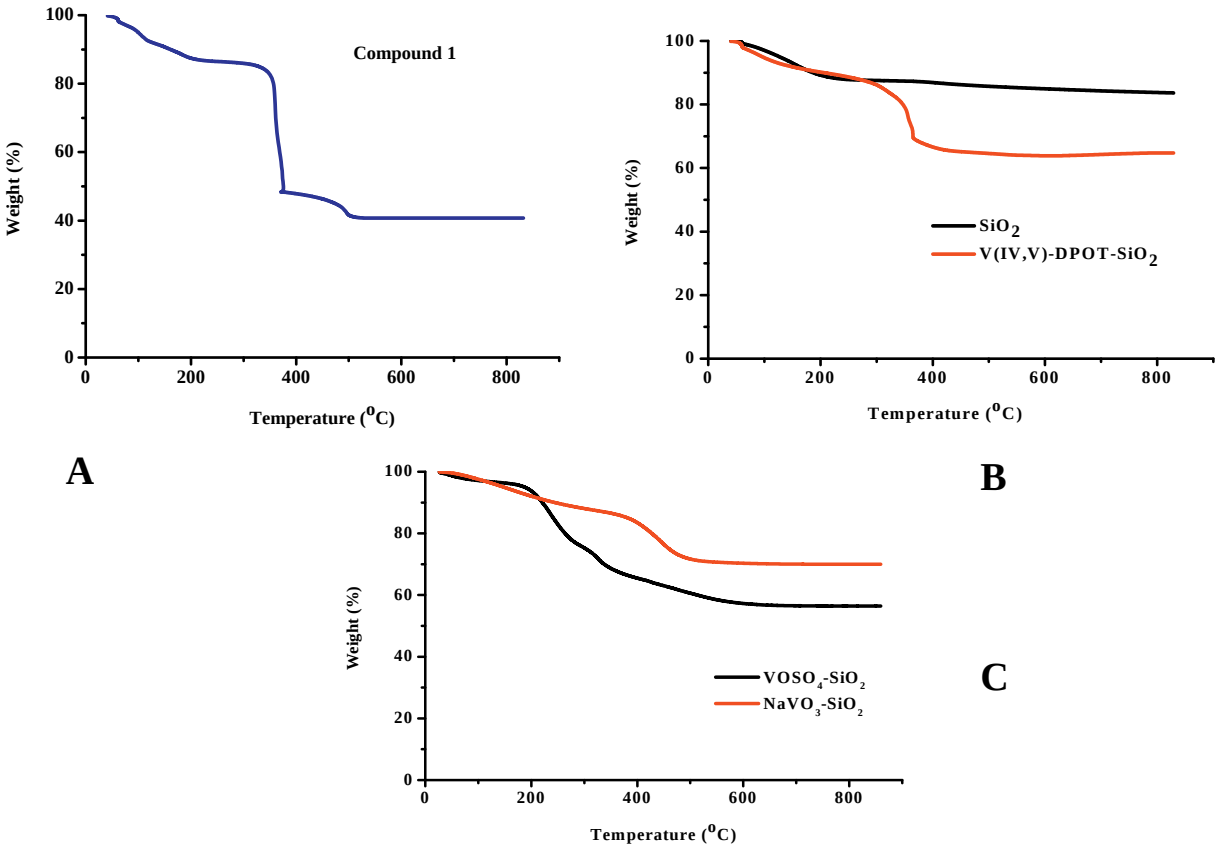

Fig. 4. TGA diagrams of **A) 1**, **B)** SiO_2 NPs and (V(IV,V)-DPOT)-SiO_2 NPs, and **C)** $VOSO_4$-SiO_2 NPs and $NaVO_3$-SiO_2 NPs.

vanadium and lithium with a ratio of 1:1, in line with the a) atomic ratio of V:Li present in the original molecular formulae, and b) presence of oxides ordinarily obtained under oxidative conditions, and consistent with previously reported results of thermogravimetric analysis on vanadium and lithium-containing species [54].

The empty silica (Fig. 4B) is thermally stable up to 61 °C and loses most of the physisorbed water molecules between 50 °C and 190 °C. At higher temperatures, between 190 °C and 635 °C, the observed weight loss is mainly attributed to the condensation of silanols [55], the subsequent burning of residual organic molecules [56], and crystallization phenomena [57].

The V(IV,V)-DPOT-SiO_2 NP sample (Fig. 4B) is thermally stable up to 52 °C and loses most of the physisorbed water molecules between 52 °C and 275 °C. In the range from 275 °C to 581 °C, there is further weight loss, in line with the decomposition of the organic structure of the encapsulated molecule. A plateau is reached at 581 °C, with no further loss up to 850 °C, indicating no further condensation of silanols and/or crystallization phenomena compared to empty silica.

The $VOSO_4$-SiO_2 NP sample (Fig. 4C) is thermally stable up to 49 °C and loses most of the physisorbed water molecules between 49 °C and 177 °C. At higher temperatures, between 177 °C and 654 °C, the increased weight loss observed is due to the condensation of silanols and the subsequent burning of residual organic molecules in addition to the final stages of vanadium oxidation and further crystallization phenomena [58].

The $NaVO_3$-SiO_2 NP sample (Fig. 4C) is thermally stable up to 47 °C and loses most of the physisorbed water molecules between 47 °C and 211 °C. The second weight loss is observed between 211 °C and 367 °C, and results from the combustion and oxidative decomposition of the organic species in the air flow. The third weight loss, observed between 367 °C and 616 °C, is ascribed to the loss of water via condensation of silanol groups to form siloxane bonds and the continuing loss of residual hydrocarbon [59].

3.7. X-ray diffraction patterns

The diffraction patterns of SiO_2 NPs, $VOSO_4$-SiO_2 NPs, and $NaVO_3$-SiO_2 NPs are shown in Fig. 5A–C. SiO_2 displays only amorphous features, whereas the $VOSO_4$-SiO_2 and the $NaVO_3$-SiO_2 samples exhibit sharp crystalline peaks on top of the amorphous SiO_2 humps. For the $VOSO_4$-SiO_2 sample, the peaks are identified as $VOSO_4 \cdot 3H_2O$ and indexed in the monoclinic $P2_1/n$ (14) space group, according to JCPDS-ICDD Powder Diffraction File 72-912. Least-squares refined cell parameters of the $VOSO_4$-SiO_2 NP sample are a = 7.3831(12) Å, b = 7.3989(11) Å, c = 12.046(2) Å and β = 106.60(1)°. For the $NaVO_3$-SiO_2 NP sample, the peaks at low temperature form β-$NaVO_3$ and are indexed in the orthorhombic *Pnma* space group, according to JCPDS-ICDD Powder Diffraction File #32-1198. Least-squares refined cell parameters of the $NaVO_3$-SiO_2 NP sample are a = 14.1386(11) Å, b = 3.6499(5) Å, c = 5.3694(5) Å. The unidentified peaks at 2θ = 24.15° (d = 4.63 Å) and 2θ ≈ 29.5° (d ≈ 3.8 Å) are attributed to residual organic species.

3.8. SEM analyses

The morphology of all samples was studied by scanning electron microscopy. Fig. 6A–C portrays SEM micrographs of the morphology of $VOSO_4$-SiO_2 NP, NaO_3V-SiO_2 NP, and (V(IV,V)-DPOT)-SiO_2 NP samples, respectively. As shown in Fig. 6A–C, size varies from 750 to 900 nm and there is no significant change in size between samples, despite the differences in the type of the encapsulated vanadium compound and encapsulation efficiency of each compound. All types of vanadium-loaded SiO_2 NPs are well-defined, lamellar and overly dense particles with polygonal shapes, sharp edges and intense crackles, constituting micro-sized agglomerates. The observed increased diameter of the particles is mostly due to the relatively high encapsulation load and high viscosity of the reaction emulsion [60].

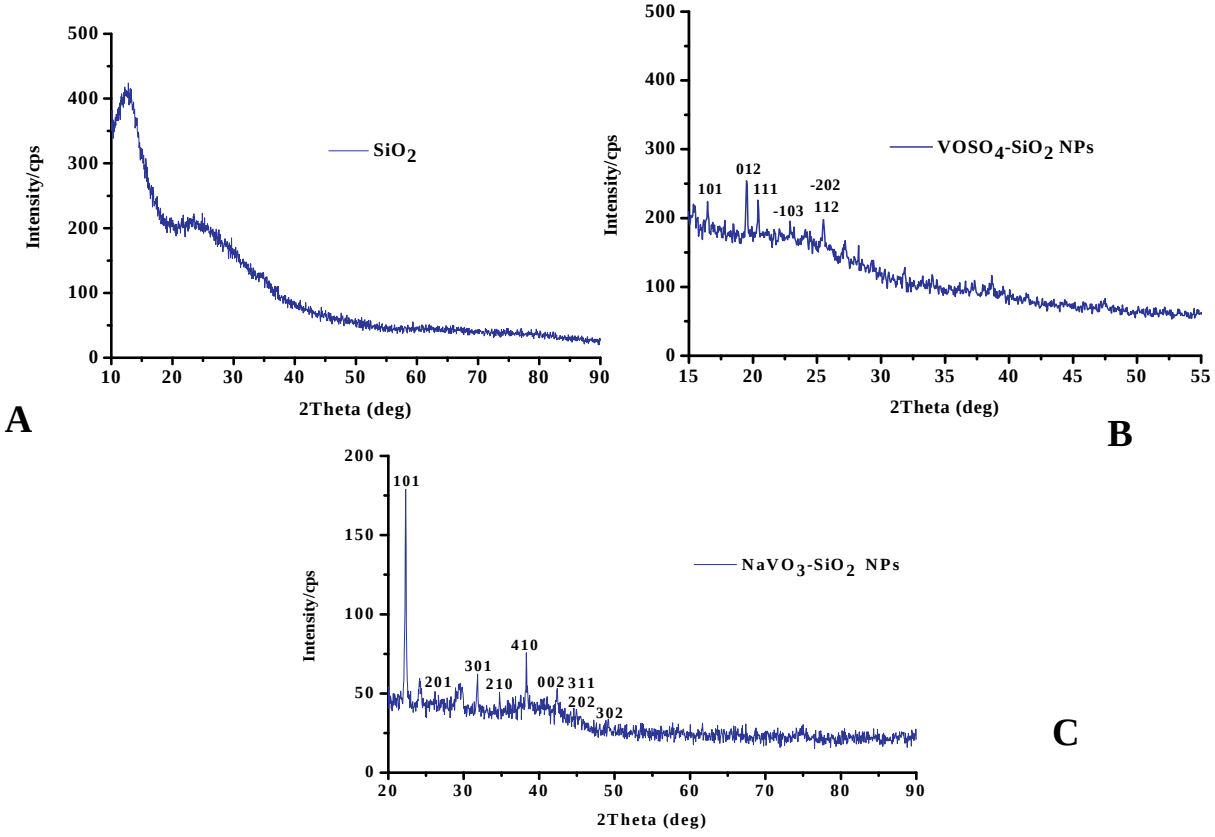

Fig. 5. XRD patterns of: **A)** SiO_2 NPs, **B)** $VOSO_4$-SiO_2 NPs, and **C)** $NaVO_3$-SiO_2 NPs.

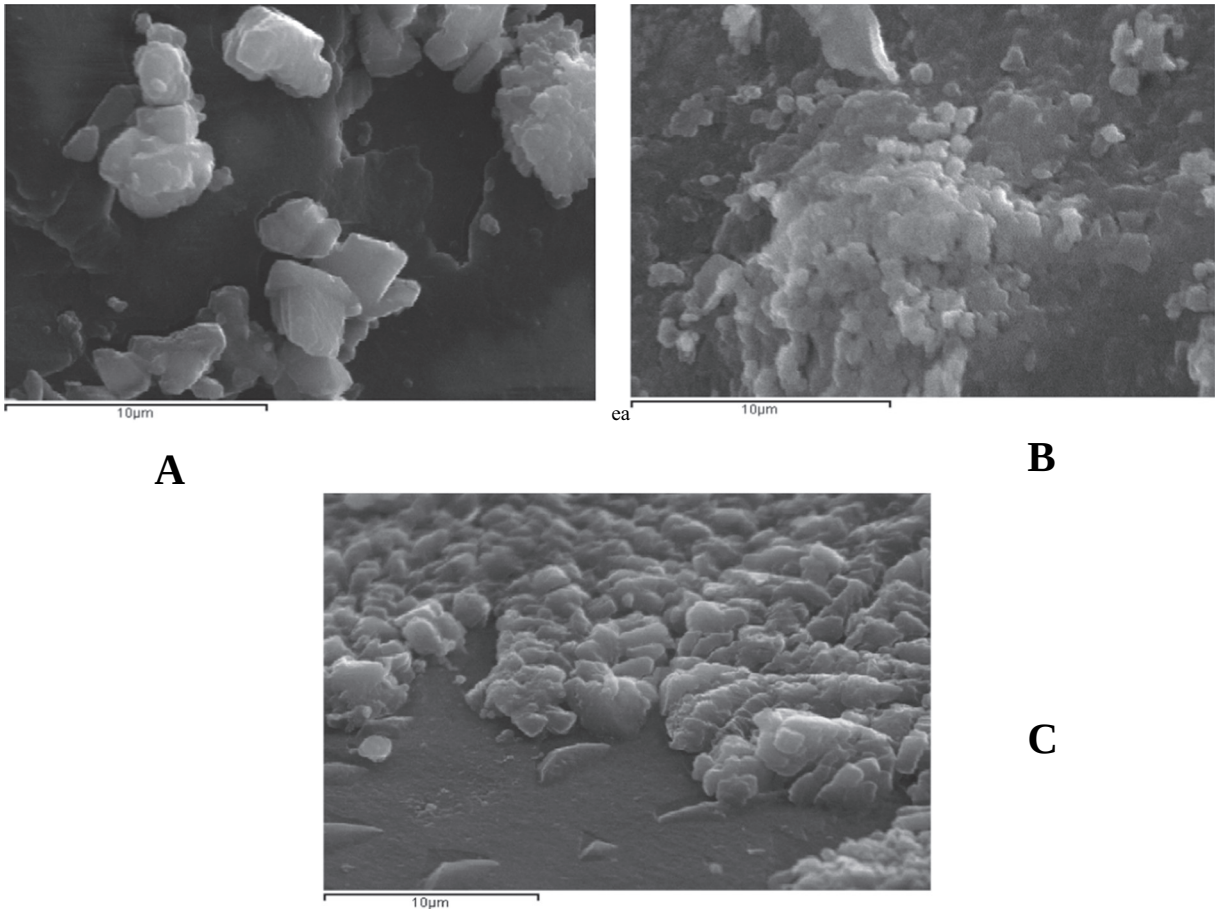

Fig. 6. SEM images of: **A.** $VOSO_4$-SiO_2 NPs at 10 μm, **B.** $NaVO_3$-SiO_2 NPs at 10 μm, and **C.** (V(IV,V)-DPOT)-SiO_2 NPs at 10 μm.

3.9. BET analyses

N_2 adsorption isotherms and pore size distribution of the samples SiO_2, $VOSO_4$-SiO_2, $NaVO_3$-SiO_2 and (V(IV,V)-DPOT)-SiO_2 are reported in Fig. 7A and B, respectively. The isotherms of all samples are of type II and more specifically type IIa, according to the IUPAC classification [61], a type associated with monolayer-multilayer adsorption on a non-porous or macroporous powder. The $VOSO_4$-SiO_2, $NaVO_3$-SiO_2, and (V(IV,V)-DPOT)-SiO_2 samples exhibit an increase in adsorption at low P/P_o and a well-defined knee (point B) indicative of monolayer completion. A less steep increase in adsorbed amounts follows; a sign of multilayer adsorption mechanism. Finally, at high P/P_0, the adsorbed amounts increase asymptotically to very high values without reaching a plateau as shown in Fig. 7A. Calculated BET surface areas are low for $VOSO_4$-SiO_2 NP, $NaVO_3$-SiO_2 NP, and (V(IV,V)-DPOT)-SiO_2 NP samples, with values between 15.60 and 19.20 $m^2 \cdot g^{-1}$, indicating that the NPs are aggregated extensively, thereby making a large part of the surface of the particles inaccessible to N_2 molecules. This aggregation is also confirmed through the SEM images. In contrast, SiO_2 NPs adsorb larger amounts of N_2, leading to a higher surface area value of 55.20 $m^2 \cdot g^{-1}$. Pore volumes are usually calculated from isotherms based on the adsorbed amounts at $P/P_0 = 0.99$. For type II isotherms the calculation is hardly applicable, since isotherms reach asymptotically very high adsorbed amounts, leading to unrealistically high pore volumes. An alternative way to determine pore volumes, V_p, is by applying the Barrett, Joyner and Halenda (BJH) method for pore size distribution (PSD) (Table 3). The micropore volumes, V_μ, calculated through the Dubinin-Raduschevich method are even lower. Based on these results, the mean pore diameter of the samples can be calculated from $2V_p/S_{BET}$ (Table 3). Finally, the PSD by the BJH method is given in Fig. 7B and shows that pore sizes fall in the mesopore region (i.e. 60–150 Å) [62]. Collectively, samples can be considered to be, for all practical purposes, macroporous, with a low percentage of mesopores and negligible microporosity. These data demonstrate that the presence of the encapsulated vanadium compounds has the main effect of modifying the silica pore size distribution, by reducing the micropore volume of the silica framework, even upon incorporation of low amounts of vanadium [42].

3.10. Entrapment efficiency

The in situ loading efficiency of the $VOSO_4$-SiO_2 NP and $NaVO_3$-SiO_2 NP samples was estimated to be 31.2% and 45.8%, respectively, whereas the storage capacity for V(IV,V)-DPOT-loaded SiO_2 NPs was 23.5%. The difference in the encapsulation efficiency between the $VOSO_4$-SiO_2 NP and $NaVO_3$-SiO_2 NP samples is mainly due to the different type of catalyst used during the hydrolysis reaction of the alkoxide. Basic conditions increase the hydrolysis reaction rate as more alkoxide groups are hydrolyzed, leading to branched polymer products of higher encapsulation capacity. In addition, condensation reactions, under basic conditions, increase the rigidity of the Si—O—Si network. Drying of silica results in dehydration, as Si—O—H groups change to Si—O—Si groups, thus developing a well-organized silica network. All of these structural rearrangements increasingly affect vanadium dispersion into the bulk network [63–65]. The low encapsulation capacity of the V(IV,V)-DPOT-loaded SiO_2 NPs, compared to the other two samples, is probably due to the a) avoidance of catalyst addition during the synthetic procedure, resulting in a limited degree of alkoxide hydrolysis, and b) bulky size of the structure of V(IV,V)-DPOT complex, which may have prevented formation of strong Si—O—V bonds.

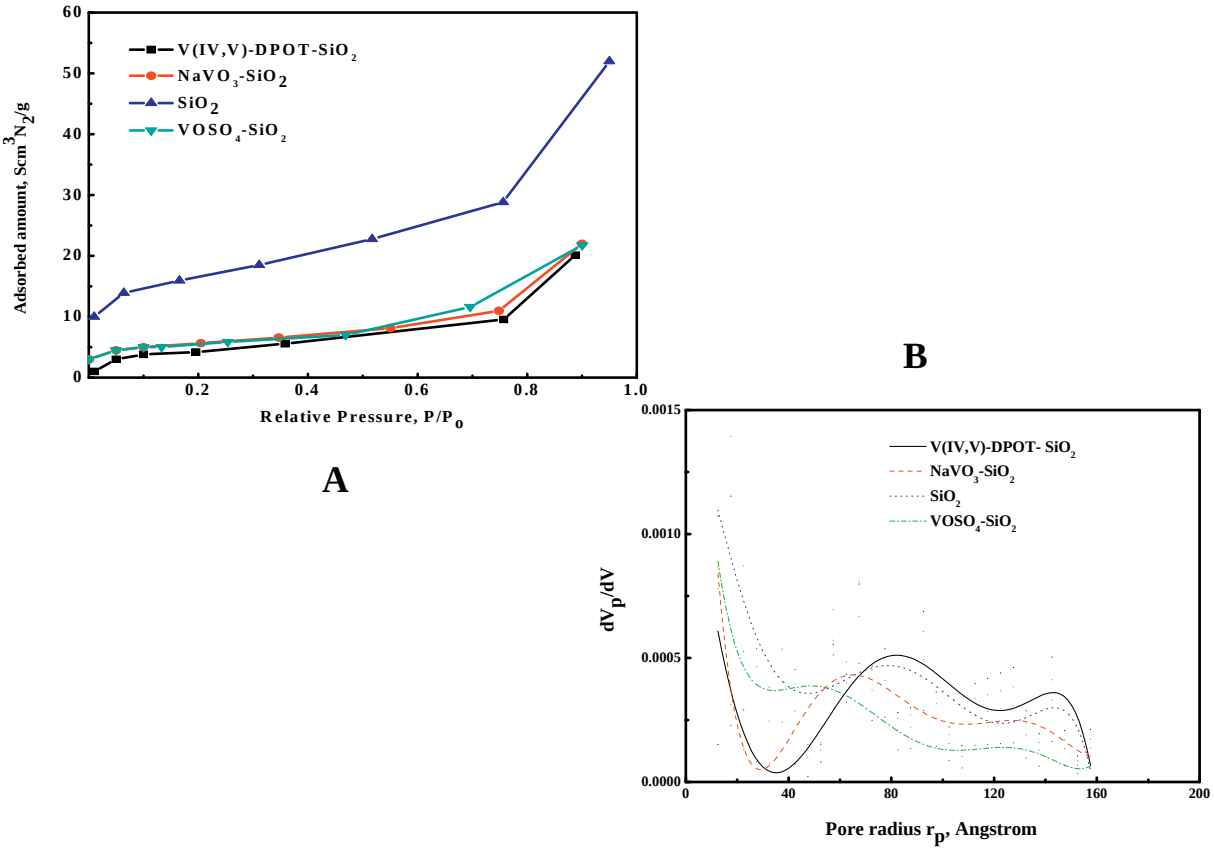

Fig. 7. A. Nitrogen adsorption isotherms of SiO_2 NPs, $VOSO_4$-SiO_2 NPs, $NaVO_3$-SiO_2 NPs, and V(IV,V)-DPOT-SiO_2 NPs. **B.** Pore size distribution of SiO_2, $VOSO_4$-SiO_2 NPs, $NaVO_3$-SiO_2 NPs and (V(IV,V)-DPOT)-SiO_2 NPs.

Table 3
Pore structure characteristics of the samples.

Sample	S_{BET}, $m^2 \cdot g^{-1}$	V_p (BJH), $cm^3 \cdot g^{-1}$	r_p, Å	V_μ, $cm^3 \cdot g^{-1}$
(V(IV,V)-DPOT)-SiO_2 NPs	15.6	0.047	60.2	0.0018
$NaVO_3$-SiO_2 NPs	19.2	0.041	42.7	0.0035
SiO_2	55.2	0.062	23.8	0.0093
$VOSO_4$-SiO_2 NPs	18.5	0.026	28.1	0.0031

3.11. Release study

The release profile of each active V(IV), V(V) or V(IV,V) ingredient of the loaded NPs is an important parameter, since it modulates the pharmacokinetic behavior of the three types of vanadium compound-loaded SiO_2 NPs. In terms of evaluating the release profile, two factors should be taken under consideration: the total amount of vanadium compound released and the rate of release vs time. Fig. 8A and B shows the concentration ($mg \cdot g^{-1}$) of vanadium compound released vs time and the percentage of vanadium compound released with regard to the total entrapped vanadium compound vs time, respectively, for the three types of vanadium-loaded SiO_2 NPs. The equilibrium release amount from $VOSO_4$-loaded sample was estimated to be 6.6 mg per 0.1 g product, and the corresponding results for $NaVO_3$ and (V(IV,V)-DPOT)-loaded SiO_2 NPs, were estimated to be 9.5 and 9.4 mg per 0.1 g product, respectively. The equilibrium cumulative vanadium compound release percentage from $VOSO_4$-loaded samples was estimated to be 93.0% and the corresponding results for $NaVO_3$ and V(IV,V)-DPOT-loaded SiO_2 NPs were estimated to be 59.8% and 75.2%, respectively. The internal and external structures of porous silica nanospheres as well as interactions between the vanadium compounds and the silica matrix affect the cumulative release percentages. The elevated percent release of $VOSO_4$-loaded samples can be attributed to the significant entrapment efficiency and high aqueous solubility of $VOSO_4$. In the case of (V(IV,V)-DPOT)-loaded SiO_2 NPs, the bulkier structure of V(IV,V)-DPOT complex weakens the interactions between the vanadium compound and the silica matrix, thus contributing to the increase of the release percentage [66]. As a result, more V(IV,V)-DPOT molecules exist on the silica surface that can come in direct contact with the release medium. Examination of the release profiles from all samples over a period of 48 h, testified to the identity and integrity of the released vanadium compounds and proved that the rate of vanadium compound release took place faster up to about 60 min, then the process got slower and the rates decreased significantly. The (V(IV,V)-DPOT)-SiO_2 sample exhibits the highest rate of release within the first hour, indicating the existence of an extensive number of surface-absorbed V(IV,V)-DPOT molecules that come directly in contact with the release medium.

3.12. UV–Vis measurements

The electronic spectra (Fig. 9) of **1** and (V(IV,V)-DPOT)-SiO_2 were recorded in ultrapure H_2O. The (V(IV,V)-DPOT)-SiO_2 sample was stirred for 24 h in a closed vessel before measurement, in order to achieve complete release of the encapsulated compound according to the release study experiment (vide supra). The spectrum of **1** (λ_{max} = 748 nm, $\varepsilon \approx 710\ M^{-1}\ cm^{-1}$) contains absorption bands at 593 nm, 620 nm, and 748 nm, which can be attributed to d-d transitions of V(IV) and absorption bands at 231 nm, 369 nm and 414 nm, conventionally attributed to ligand to metal charge-transfer (LMCT) transitions of the O → V(V) type [67,68]. In the case of the (V(IV,V)-DPOT)-SiO_2 NP spectrum, the bands attributed to d-d transitions of V(IV) are retained (590 nm and 748 nm), thus indicating the successful

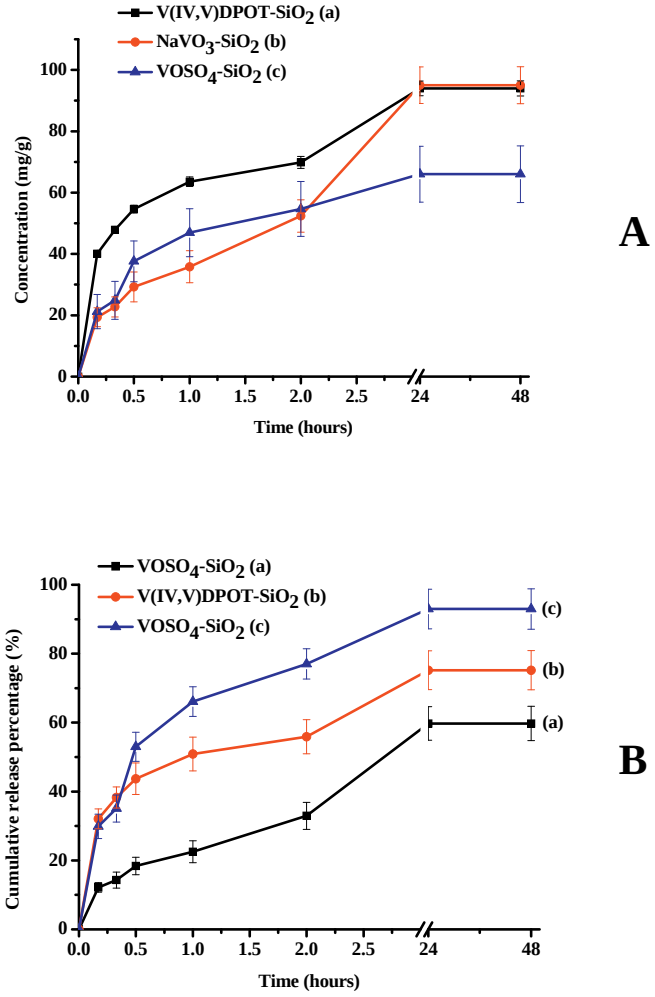

Fig. 8. A. Cumulative released $VOSO_4$, $NaVO_3$, and V(IV,V)-DPOT concentration, vs time, for $VOSO_4$-SiO_2 NPs, $NaVO_3$-SiO_2 NPs, and (V(IV,V)-DPOT)-SiO_2 NPs, respectively.
B. Cumulative release percentage of $VOSO_4$, $NaVO_3$, and V(IV,V)-DPOT, with regard to the total entrapped $VOSO_4$, $NaVO_3$, and V(IV,V)-DPOT, vs time, for $VOSO_4$-SiO_2 NPs, $NaVO_3$-SiO_2 NPs, and (V(IV,V)-DPOT)-SiO_2 NPs, respectively.

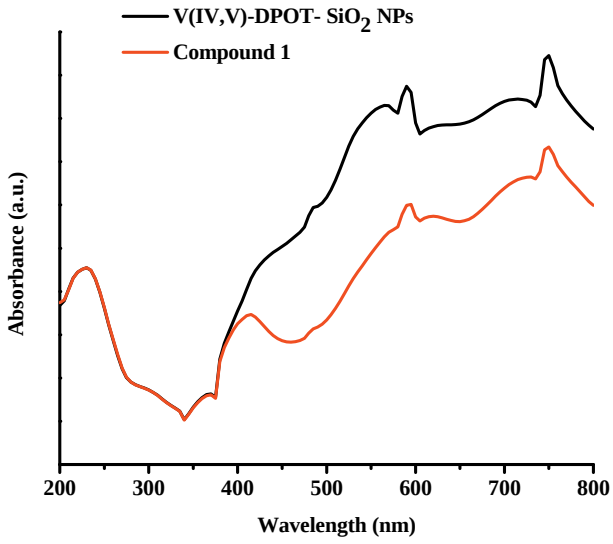

Fig. 9. UV–Visible spectra of **1**, and (V(IV,V)-DPOT)-SiO_2 NPs in H_2O.

encapsulation of **1** inside the silica matrix. The spectra of the non-encapsulated and encapsulated vanadium compound in water suggest that the same species emerge in solution and likely arise from the same solid state species (free and encapsulated). Absorption bands at 567 nm and 590 nm are also indicative of the presence of octahedrally coordinated (group O_h) 2D/3D bulk-like VO_x units [69,70]. The disappearance of the absorption band at 414 nm in the spectrum of (V(IV,V)-DPOT)-SiO_2 NPs sample indicates that a certain amount of compound **1** molecules are adsorbed onto the SiO_2 substrate and contain V=O centers interacting with surface oxygen moieties of the silica matrix [71].

3.13. Reactive oxygen species (ROS) assay of free and SiO_2-encapsulated vanadium compounds

Upon determination of intracellular and extracellular reactive oxygen species – specifically superoxide anion radicals ($O_2^{\cdot -}$) - levels in the presence of free and SiO_2-encapsulated vanadium compounds, the findings revealed a distinct profile for each compound used, depending on the bacterial species employed (Figs. 10–12, Tables S1–S6). ROS determination of free SiO_2 NPs showed no particular activity (data not shown). The intracellular (IN) ROS levels in BS (Fig. 10A, Table S1), caused by the presence of $VOSO_4$, in the concentration range 0.5–25 μg·mL^{-1}, decreased gradually to 55.9%, with the corresponding extracellular (EX) ROS values, following the same trend down to 65.7% at the highest employed concentration, compared to control. At the same $VOSO_4$ concentrations, the intracellular ROS determination in EC showed a gradual decrease to 57.4%, with the corresponding extracellular ROS measured value standing at 63.9% for the highest employed concentration, compared to control.

In the same concentration range 0.5–25 μg·mL^{-1}, the intracellular ROS profile of $VOSO_4$-SiO_2 NPs in BS exhibited a gradual reduction reaching a value of 46.5%, with its extracellular profile showing the same trend down to 54.1% at the highest employed concentration, compared to control (Fig. 10B, Table S2). In contrast to that, for the same concentrations, the ROS patterns for $VOSO_4$-SiO_2 NPs in EC reflected a gradual decrease down to 52.0% intracellularly, and a final value of 52.7%, extracellularly, at the highest employed concentration, compared to control.

The ROS intracellular (IN) levels of the V(IV,V)-DPOT compound in the concentration range 0.5–25 μg·mL^{-1} in BS (Fig. 11A, Table S3) decreased to a final 70.7%, with the corresponding extracellular (EX) level being 73.9% at the highest employed concentration, compared to control. For the same V(IV,V)-DPOT compound concentrations, in EC, the intracellular ROS levels were recorded decreasing to 75.1% vs the corresponding extracellular levels, reaching a final value of 73.3% at the highest employed concentration, compared to control.

At (V(IV,V)-DPOT)-SiO_2 NP concentrations in the range 0.5–25 μg·mL^{-1} (Fig. 11B, Table S4), intracellular ROS values decreased gradually to 57.0% vs the extracellular values in BS, which followed a similar trend down to a final value of 63.9%, at the highest employed concentration, compared to control. For the same (V(IV,V)-DPOT)-SiO_2 NP concentrations, the intracellular ROS levels in EC decreased progressively to 61.8%, as opposed to the extracellular levels, which followed the same trend, finally reaching 63.2%, at the highest employed concentration, compared to control.

The intracellular (IN) ROS levels caused by $NaVO_3$ in the concentration range 0.5–25 μg·mL^{-1} (Fig. 12A, Table S5), in BS, decreased gradually to 80.5%, with the extracellular (EX) ROS levels following the same trend, finally reaching a value of 85.7%, at the highest employed concentration, compared to control. In the case of EC, for the same concentrations, the intracellular ROS levels decreased progressively to 78.4% vs the extracellular levels, following the same trend and finally reaching a value of 83.0%, at the highest employed concentration, compared to control.

The $NaVO_3$-SiO_2 NP samples (Fig. 12B, Table S6), in the concentration range 0.5–25 μg·mL^{-1}, showed that the intracellular ROS

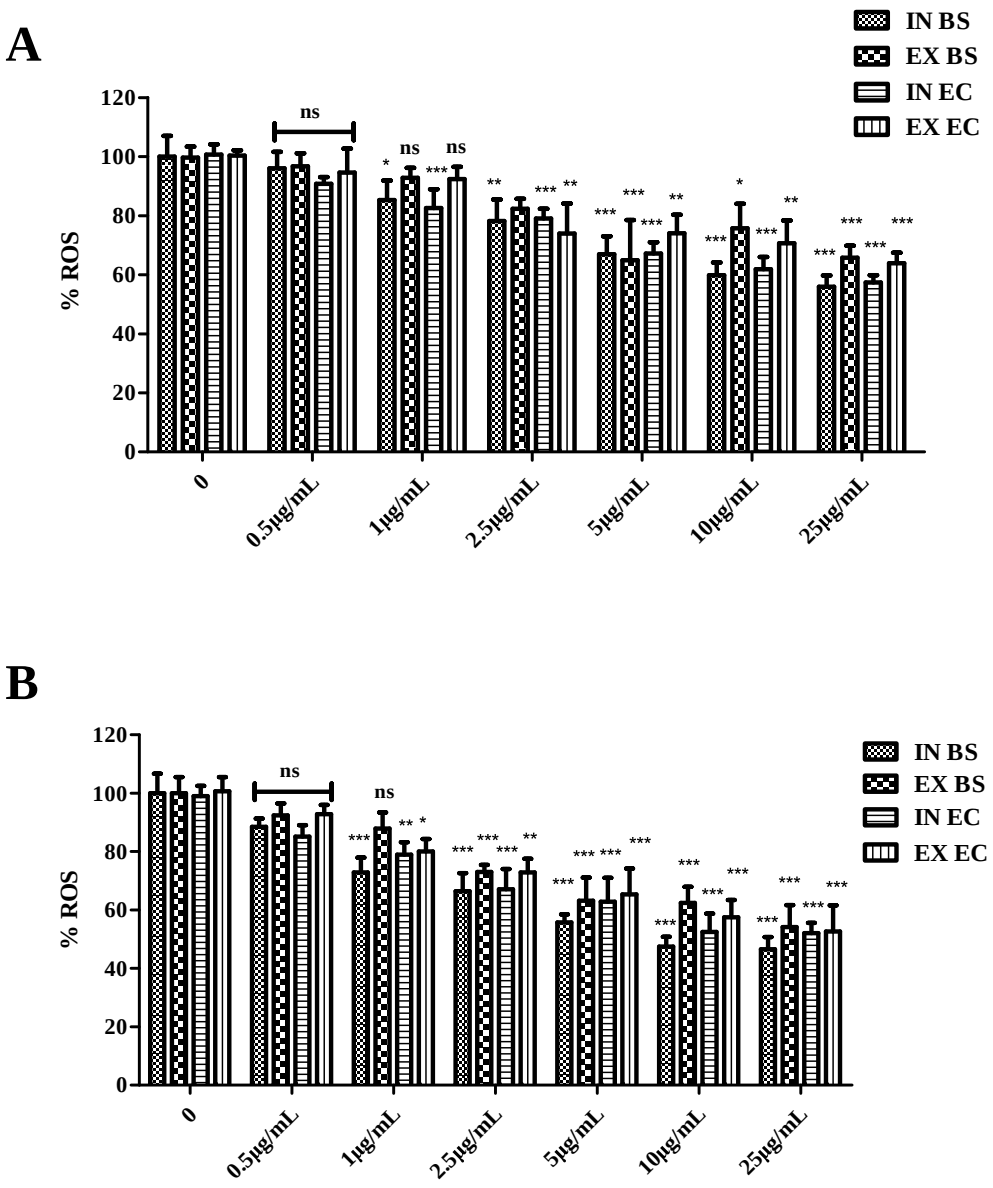

Fig. 10. Reactive oxygen species (%ROS) profile in the presence of **A.** $VOSO_4$, and **B.** $VOSO_4$-SiO_2 NPs. IN, intracellular; EX, extracellular. Vertical bars represent SEMs. *: $p < 0.05$; **: $p < 0.01$; ***: $p < 0.001$ vs control.

levels, in BS, decreased with rising concentrations to 67.5% vs the extracellular ROS levels, following the same trend and finally reaching a value of 68.0%, at the highest employed concentration, compared to control. Upon incubation of EC in the presence of $NaVO_3$-SiO_2 NPs with the same nanoparticle concentrations, ROS intracellular values decreased gradually down to 64.0% vs the extracellular levels following a similar trend and finally reaching a value of 68.7%, at the highest employed concentration, compared to control. In general, intra- and extracellular ROS patterns varied among free and SiO_2-encapsulated vanadium compounds.

3.14. Evaluation and comparison of Radical Scavenging Capacity (RSC) of free and SiO_2-encapsulated vanadium compounds

The antiradical scavenging capacity of all types of free and SiO_2-encapsulated vanadium compounds used in this study was evaluated through the DPPH assay and presented in Fig. 13 (Table S7). Specifically, samples of $VOSO_4$, V(IV,V)-DPOT, $NaVO_3$, and SiO_2 were run for comparison with the results of vanadium-loaded SiO_2 NPs, $VOSO_4$-SiO_2 NPs, (V(IV,V)-DPOT)-SiO_2 NPs, and $NaVO_3$-SiO_2 NPs. RSC measurements of the $VOSO_4$ compound were recorded at 30.4, 40.9, 50.9, 95.4, and 97.2% at 10, 20, 40, 100, and 150 $\mu g \cdot mL^{-1}$, respectively, and at 25.4, 35.9, 45.9, 90.4, and 95.2% at 10, 20, 40, 100, and 150 $\mu g \cdot mL^{-1}$, respectively, for its encapsulated form of the $VOSO_4$-SiO_2 NP sample (Fig. 13A). The RSC capacity of the V(IV,V)-DPOT compound was recorded at 9.0, 22.0, 42.9, 59.0, and 48.9% at concentrations of 10, 20, 40, 100, and 150 $\mu g \cdot mL^{-1}$, and the RSC capacity of (V(IV,V)-DPOT)-SiO_2 NP samples showed 21.0, 34.0, 61.2, 80.3, and 83.9% at the same aforementioned concentrations, correspondingly (Fig. 13B). Surprisingly, the RSC values of $NaVO_3$ were 6.2, 7.4, 18.6, 8.0 and 7.1% and the RSC values of $NaVO_3$-SiO_2 NP samples stood at 10.5, 19.3, 46.5, 33.0 and 32.6% for concentrations of 10, 20, 40, 100, and 150 $\mu g \cdot mL^{-1}$, respectively (Fig. 13C). Negligible RSC values were observed for empty SiO_2 NPs, suggesting a non-direct interference with the encapsulated vanadium compounds. Overall, the results formulated the differential antiradical profile of vanadium compounds and vanadium-loaded SiO_2 NPs samples.

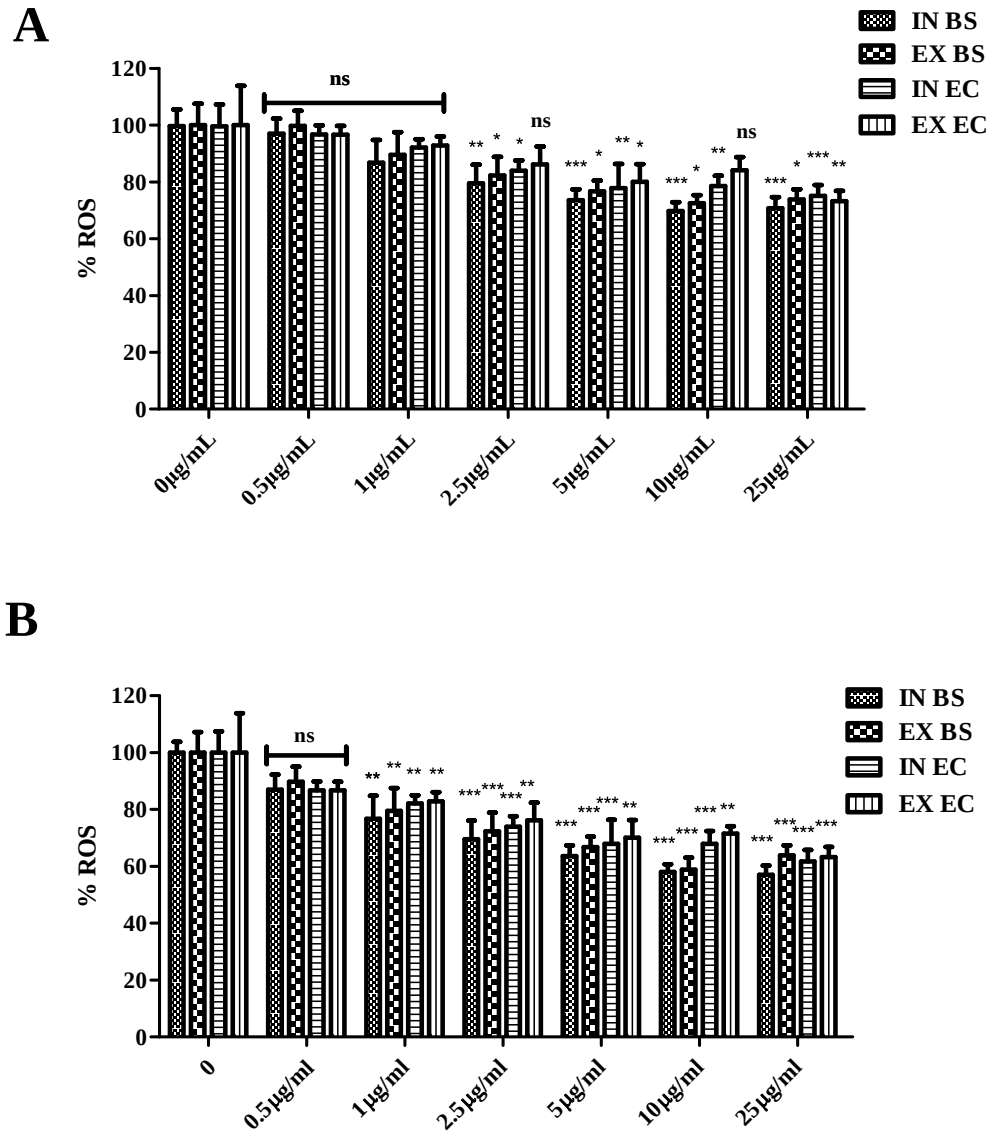

Fig. 11. Reactive oxygen species (%ROS) profile in the presence of **A.** V(IV,V)-DPOT, and **B.** (V(IV,V)-DPOT)-SiO_2 NPs. Designations: IN, intracellular; EX, extracellular. Vertical bars represent SEMs. *: $p < 0.05$; **: $p < 0.01$; ***: $p < 0.001$ vs control.

4. Discussion

4.1. Synthetic binary V(IV,V)-DPOT chemistry

In the current work, for the first time, beside the synthesis and characterization of the tetranuclear vanadium-DPOT compound, the introduction of the material in SiO_2 NPs and the associated physicochemical characterization, linked to the biological profile of its free and encapsulated forms, was the part of the work novelty linked to the synthesis of the title compound, setting the stage for the development of novel metallo-nanodrug formulations against oxidative stress conditions. In view of the fact that key biological oxidation states of vanadium include V(IV) and V(V), the a) pursuit of the synthesis of compounds bearing both specific vanadium oxidation states, and b) incorporation of individual oxidation state vanadium species, i.e. vanadyl sulfate and sodium metavanadate, in the delineation of the comparative biological profile of the title compounds (free and encapsulated in silica NPs), presents a synthetic challenge intimately linked to its biological role under the investigated experimental conditions. To that end, in aqueous solution, both vanadate and vanadyl ions undergo a number of hydrolytic and self-condensation reactions, which distinguish their aqueous chemistry from the chemistry in non-aqueous media. These reactions are very sensitive to the pH of the solution and the presence of ligands, capable of binding vanadium and forming complexes with distinct coordination geometries and properties. Complications arise, however, due to potential interconversion between oxidation states. Vanadate, under specific conditions, is also an oxidizing agent and can be readily reduced to either V(IV) or V(III). In the neutral and basic pH range, air oxidation will quickly regenerate vanadate unless V(IV) is tightly bound to efficient stabilizing ligands. Consequently, beyond the idiotypical properties of V(IV) and V(V), the choice of organic ligands (such as $DPOTH_5$ in the present study) emerges as an important factor in the construction, redox, and structural tuning of V(IV) and V(V) metal-organic compounds, given the fact that even small changes in ligand structure flexibility, length, functional group position and symmetry could result in pronouncedly different materials with diverse architectures and properties. Key ingredients in the structure of such organic ligands are a) carboxylic acid groups, alcohol and amine functionalities, heteroatoms bearing free electron pairs, capable of acting as efficient Lewis bases toward metal ions, and b) variably configured combinations of groups thereof, collectively influencing the coordination capacity, sphere, number and the

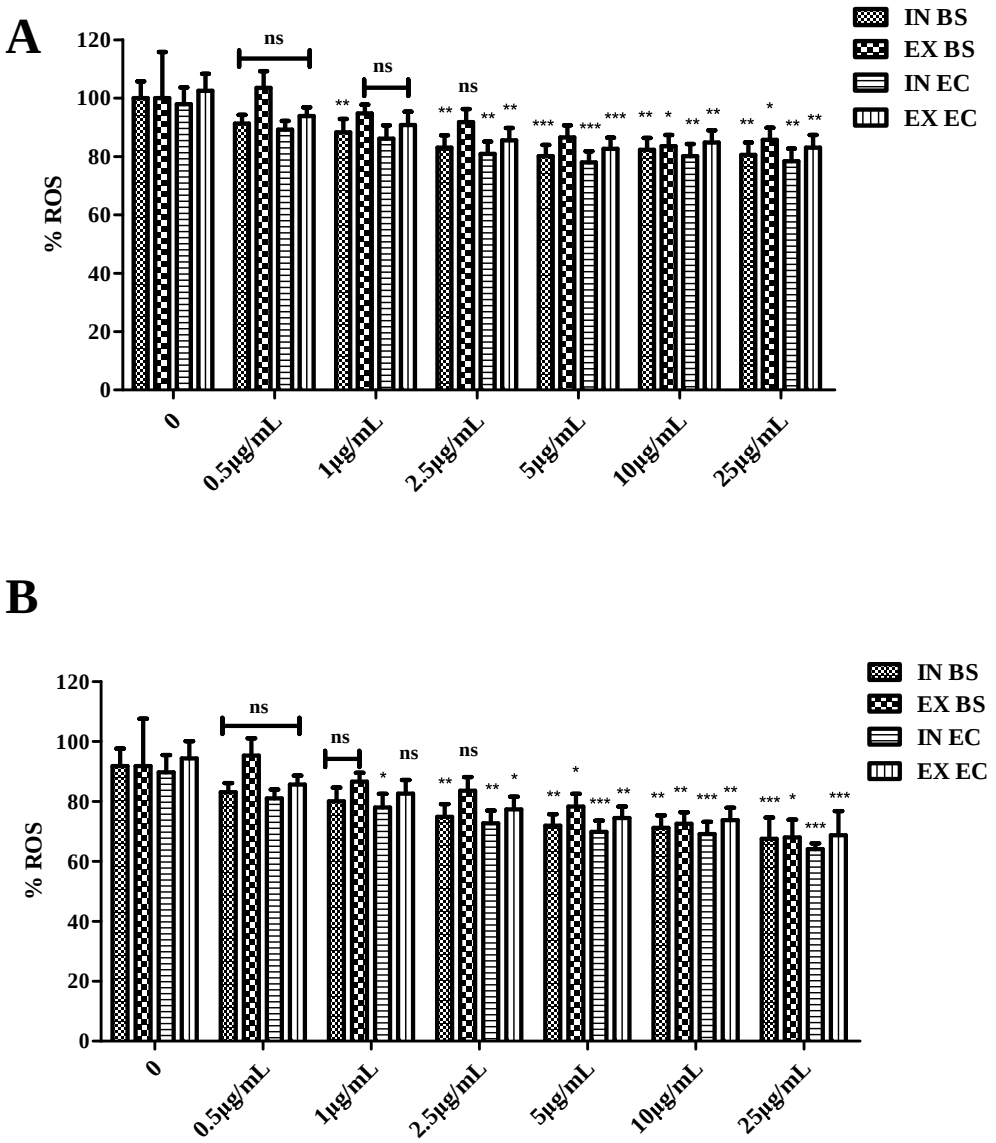

Fig. 12. Reactive oxygen species (%ROS) profile in the presence of **A.** $NaVO_3$, and **B.** $NaVO_3$-SiO_2 NPs. Designations: IN, intracellular; EX, extracellular. Vertical bars represent SEMs. *: $p < 0.05$; **: $p < 0.01$; ***: $p < 0.001$ vs control.

potential to assemble variable nuclearity hybrid structures. Among the plethorically existing organic ligands, polyaminopolycarboxylates emerge as excellent structural builders, owing to their interesting features, including strong coordination ability, diverse coordination modes of carboxylate groups, variable nature of organic skeletons and plentiful π–π interactions (when aromatic groups are involved). One such organic ligand, bearing a variable nature and number of metal binding functionalities, acting as an ancillary ligand with potential bridging role, is 1,3-diamino-2-propanol-*N*,*N*,*N*′,*N*′-tetraacetic acid (DPOT). Employment of DPOT in the present work led to the isolation of a mixed-valence V(IV,V) complex, which was subsequently isolated in crystalline form, in the presence of a counter ion involving the aquated $[Li_4(H_2O)_8]^{4+}$ complex ion. The emerging tetranuclear V-DPOT assembly, albeit known in the literature [72,73], emerged as a species containing both V(IV) and V(V) and the organic chelator $[DPOT]^{5-}$, collectively poised to enter the silica nanomatrix for further use in biologically relevant investigation(s).

Hence, the herein described efforts to pursue the synthesis of hybrid such species in the presence of lithium ions attests to the significance of the endeavor targeting heterometallic assemblies of mixed oxidation state lithium-vanadium assemblies, appropriately configured by a multidentate chelator, further enabling perusal of their potential biological activity. The ultimately afforded pure crystalline material was accounted for by the a) tetranuclear assembly consisting of dinuclear units of mixed vanadium oxidation state and bearing two fully deprotonated $[DPOT]^{5-}$ ligands, b) thermodynamically driven alkoxido-bridged moiety, bringing vanadium centers in close proximity yet different oxidation states, c) aquated lithium ions counteracting the negative charge of the tetranuclear vanadium-DPOT assembly, and d) characterization of the species to the degree justified by metal-ligand coordination and supported by spectroscopic and structural techniques (FT-IR, ESI-MS, NMR, and X-ray crystallography). The behavior of the compound in both the solid state and solution is essential in rationalizing its unique behavior at the biological level. Given the importance of a well-defined vanadium species in biological experiments, the solution properties of the V-DPOT complex along with the differences from the discrete V(IV) and V(V) species, used as control compounds, were investigated. The thus observed biological activity arises as a result of the aqueous speciation emerging upon dissolution of the title compound in water. To that end, ESI-MS spectra of the compound suggested that the tetranuclear assembly dissociates in solution, with vanadium- and lithium-ligand units prevailing in the arising complex

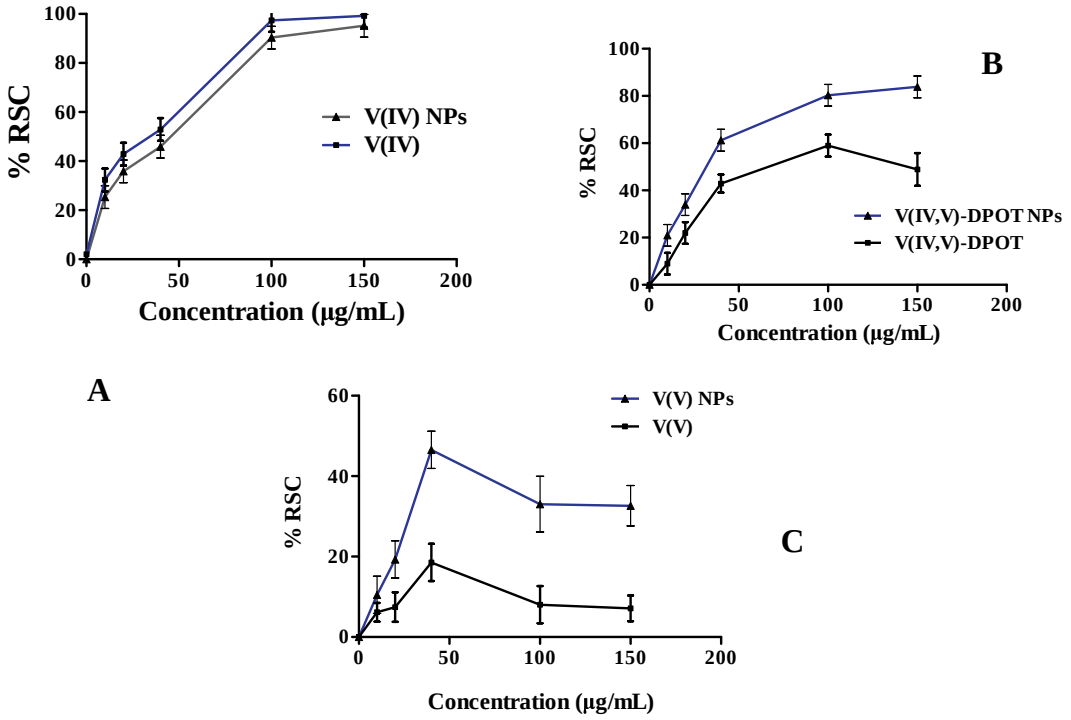

Fig. 13. Evaluation and comparison of the Radical Scavenging Capacity (%RSC) of vanadium compounds and vanadium-loaded SiO_2 NPs. **A.** $VOSO_4$ vs $VOSO_4$-SiO_2 NPs, **B.** V(IV,V)-DPOT vs (V(IV,V)-DPOT)-SiO_2 NPs, and **C.** $NaVO_3$ vs $NaVO_3$-SiO_2 NPs. Vertical bars represent SEMs.

equilibria. The electronic properties of the material in its free non-encapsulated as well as encapsulated form suggested that the UV–Visible active participants are the same and likely originate from the same assembly in the solid state, which is the tetranuclear cluster. Finally, when the tetranuclear material is subjected to repeated re-crystallizations from water or water-methanol mixtures, the product arising consistently in quantitative yields is the tetranuclear cluster in the title material **1**. The above information suggests that **1** dissociates in water yet when it returns to its solid-state form upon precipitation it assumes the thermodynamically stable state of the tetranuclear cluster. Proof of that comes from FT-IR, ^{13}C-MAS-NMR, and single crystal X-ray diffractometry of the material emerging from recrystallizations. Further work on the electrochemical properties of the arising species in solution is expected to enrich the physicochemical profile of the title compound, thus justifying its redox stability and further employment in subsequent (bio)chemical experiments. Such studies are currently ongoing in the lab. Concurrently, encapsulation of the title material in silica NPs projects the solid-state structure of the original species in its non-encapsulated form, as that is shown by ^{13}C-MAS-NMR. The slight differentiation in the low field resonance pattern of the spectrum, pertaining to the carboxylate carbonyl carbons of the bound $[DPOT]^{5-}$ ligand to vanadium centers may be indicative of the interactions of the assembly with the silica host through lithium bound water- and lattice water-mediated bridges, a suggestion also exemplified through FT-IR (vide supra). Thus, the encapsulated material in silica NPs is very likely the one used from the encapsulation process. Overall, the collective information depicts a well-defined profile of **1** in the solid state and in solution, thereby justifying its subsequent use in the ensuing biological experiments.

4.2. Vanadium encapsulation in sol-gel hosts and release profiling

The immobilization of active biomolecules within a nanoscale host offers tangible advantageous properties such as: a) optimized spatial and kinetics delivery as well as controlled release properties, b) enhancement of the solid state stability upon storage, c) improved adaptability in bio-immobilization procedures, d) nontoxic behavior, and e) extended product life cycle. The synthesized formulations enhance physiological metabolic bio-processes, maintain and protect cellular integrity, and confront pathogenetic phenotypes in an effort to remedy cellular diseases [55]. Prominent among such diseases stand oxidative stress-induced disorders. Nanoscale host agents have been proven to provide effective routes of administration through systemic barriers, such as the blood brain barrier (BBB), and into neuronal networks, profusely affected during oxidative stress conditions. In view of the fact that oxidative stress creates an imbalance between the production of free radicals and reactive metabolites, resulting in cellular degeneration, the development of an effective defensive approach stands as a plausible strategy against a progressively deteriorating condition. Cognizant of the known protective behavior of vanadium supplementation against depletion of antioxidant potency [74,75], three vanadium compounds of variable oxidation states were employed, i.e. vanadyl sulfate, sodium metavanadate and a newly synthesized V(IV,V)-DPOT complex, free and encapsulated in an appropriate stable and nontoxic inorganic matrix, such as silica NPs, for further assessment of their antioxidant and antiradical potential. To this end, the a) known antioxidant and antiradical potential of vanadium formulations, b) metal chelating ability of vanadium with polyaminopolycarboxylate (multidentate) ligands, such as DPOT, and c) synergistic interactions of V(IV,V) compounds with the siloxane matrix, were collectively shown to contribute to the V(IV,V)-DPOT SiO_2 NP potency as a nano-antioxidant and its selection in the present work. The physicochemical characterization of the hybrid nanocarriers projected a variable loading capacity of the vanadium compounds, with high release rates of their load during drug release experiments (as evidence through Flame Atomic Adsorption).

4.3. Reactive oxygen species scavenging activity of vanadium compounds versus vanadium loaded in SiO_2 NPs

Differential intracellular and extracellular ROS patterns were recorded in bacteria due to the presence of vanadium compounds and

their encapsulated forms in silica NPs. Previous investigations had focused on the role of the ligand in V(IV) and V(V) complexes to produce reactive oxygen species ($OH^{\cdot}$ and $O_2^{\cdot -}$) by Fenton and Haber-Weiss reactions [76,77]. For the first time, in this work, an intra/extracellular ROS determination was carried out using V(IV), V(IV,V), and V(V) silica nanoparticle forms compared to their non-encapsulated counterparts. To this end, the same concentration of each vanadium form (Fig. 10A) versus its nanoparticulate form (Fig. 10B) was employed in BS and EC cultures for meaningful comparisons of ROS vanadium species scavenging properties.

Specifically, a similar pattern of antioxidant response to $VOSO_4$ was observed in both BS and EC cultures with increasing V(IV) amounts (Fig. 10A). It is very likely that encapsulation of $VOSO_4$ in silica NPs projects a slightly more controlled-regulated behavior of vanadium release toward ROS in the cells (Fig. 10B), thereby enhancing the ultimate ROS lowering effect.

The V(IV,V)-DPOT compound exhibited a concentration-dependent antioxidant pattern. The antioxidant properties of the compound seemed to reflect the presence of both coordinated V(IV) and V(V) ions in the complex upon exposure in BS and EC cells (Fig. 11A). Similarly, V(IV,V)-DPOT NPs exhibited a progressively enhanced antioxidant profile (Fig. 11B) at concentrations beyond 0.5 $\mu g \cdot mL^{-1}$, tested in BS and EC cells.

Application of $NaVO_3$ (Fig. 12) on BS showed a slowly rising antioxidant response with increasing concentrations, with the trend in the rate of the antioxidant capacity projecting a plateau in the $NaVO_3$-induced antioxidant defense of the cells. A similar behavior in the antioxidant profile of $NaVO_3$ NPs was observed in BS and EC for all concentrations tested beyond 0.5 $\mu g \cdot mL^{-1}$.

Furthermore, paying close attention to the comparative behavior of each compound in its free and encapsulated form and each cell line tested, suggested that %ROS reduction differential patterns between corresponding experimental conditions could be extracted for all vanadium compounds examined (within experimental error). Specifically, considering the strongest effect seen at the highest vanadium concentration examined (25 $\mu g \cdot mL^{-1}$) in the case of BS cells exposed to $VOSO_4$ vs $VOSO_4$ NPs, the intracellular %ROS reduction upon employment of $VOSO_4$ NPs was 9.4% vs 11.6% in the case of the extracellular %ROS reduction. The corresponding effect in the case of EC cells was 5.4% vs 11.2%. In the case of V(IV,V)-DPOT vs V(IV,V)-DPOT NPs, the differential intracellular vs extracellular %ROS reduction in BS cultures was 13.7% vs 10.0%. The corresponding effect in the case of EC cells was 13.3% vs 10.0%. Finally, in the case of $NaVO_3$ vs $NaVO_3$ NPs, the differential intracellular %ROS reduction upon employment of $NaVO_3$ NPs was 13.0% vs 17.7% in the extracellular case. The corresponding effect in the case of EC cells was 14.0% vs 14.4%. It appears therefore, that a) encapsulation of $VOSO_4$ induces a higher reduction of the extracellular ROS levels compared to the intracellular ones in both BS and EC cultures. The effect was more pronounced in the case of the EC cells; b) employment of V(IV,V)-DPOT NPs resulted in higher reduction of the intracellular vs extracellular ROS levels in both BS and EC cultures. Undoubtedly the activity of these nanoparticles was higher than that of $VOSO_4$; and c) the $NaVO_3$ NP behavior showed high %ROS reduction in both BS and EC cultures, with a significant reduction occurring in the extracellular ROS levels of the BS cells. Overall, the observed antioxidant patterns emerging for the V(IV), V(IV,V)-DPOT, and V(V) compounds, suggest that the concurrent presence of V(IV) and V(V) in V(IV,V)-DPOT plays a significant role in the formulation of the biological activity. Encapsulation of the material in NPs appears to enhance that activity. This enhancement projects an increase in %ROS neutralization compared to $VOSO_4$, a) intracellularly, and b) concurrently being similar to that observed in $NaVO_3$. The observed behavior suggests that the structurally configured, mixed oxidation state, V(IV,V)-DPOT compound possesses biological properties supporting the antioxidant status in both BS and EC cells, concurrently mitigating any adverse effects arising from the fully oxidized form of V(V) in $NaVO_3$ (vide infra). Further in-depth assessment of reactive oxygen species production, under such experimental conditions as the ones used in this work involving vanadium species (free and in encapsulated forms in loaded NPs), through EPR spectroscopy and spin-trapping approaches, is expected to usher in more detailed information on the issue of antioxidant activity counteracting oxidative stress and is currently researched in our lab.

4.4. Radical Scavenging Capacity properties of free and SiO_2-encapsulated vanadium

The differential antiradical profile of the free and SiO_2-encapsulated vanadium compounds was evaluated using the radical scavenging capacity DPPH assay (Fig. 13). It's worth noting that, based on previous work, use of DPPH in organic or mixed aqueous methanolic media with low content in water, lead to reliable results, representative of those purported to be taking place in aqueous media, with the involved title materials and DPPH gaining full accessibility to the targets involved in the antioxidant assay [78]. To that end, EPR studies support that contention, thereby providing credence to the a) use of the employed experimental conditions (including the solvent system(s)) for the evaluation of the antioxidant potential of the title compounds, and b) evaluation of the RSC activity in the context of the herein conducted research. The vanadium compounds used included $VOSO_4$, V(IV,V)-DPOT, $NaVO_3$ along with their corresponding silica NPs. The rationale and justification of their employment stands on the fact that vanadyl sulfate a) was the precursor employed in the synthetic procedure of the V(IV,V)-DPOT title compound, b) was also used as the source of vanadyl ions V(IV) encapsulated in the silica matrix of the nanoparticles synthesized and subsequently used in biological experiments, c) served as a control to the title compound, with respect to the biological behavior observed, and d) was further tested for its discrete antioxidant and antiradical potential. By the same token, sodium metavanadate was employed as the source of vanadate ions V(V), also encapsulated in the silica matrix, thereby giving rise to the corresponding NPs, subsequently used in the biological experiments as comparative control species.

For the first time, an antiradical investigation was carried out into encapsulated V(IV) $VOSO_4$ and V(V) $NaVO_3$ compounds. Based on the observations, $VOSO_4$ was the most potent antiradical agent among the vanadium compounds used, i.e. $VOSO_4$, V(IV,V)-DPOT, $NaVO_3$, $VOSO_4$ NPs, V(IV,V)-DPOT NPs, and $NaVO_3$ NPs, at all concentrations tested (Fig. 13A). The antiradical activity of free V(IV,V)-DPOT was < 60% at concentrations of 100 and 150 $\mu g \cdot mL^{-1}$. On the other hand, the encapsulated V(IV,V)-DPOT NP antiradical activity was ~80% at the highest concentrations of 100 and 150 $\mu g \cdot mL^{-1}$. In this case, the antiradical performance of the NPs was likely enhanced by the fortified bioavailability of V(IV,V)-DPOT encapsulated in the silica NPs compared to V(IV,V)-DPOT alone (Fig. 13B). The antiradical activity of V(V), in free $NaVO_3$, was lower than 20% for all three higher concentrations tested. A better antiradical profile was observed for its encapsulated form, reaching higher than 46% of the RSC at 40 $\mu g \cdot mL^{-1}$. This steep, > 100%, increase in %RSC, may reflect a more targeted and controlled release of that inorganic form of vanadium from the silica nanoparticles in relation to non-encapsulated vanadium (Fig. 13C). It appears, therefore, that the observed %RSC levels for the non-encapsulated V(IV,V)-DPOT as well as V(IV,V)-DPOT NPs are between those observed for $VOSO_4$ and $NaVO_3$ as well as their NP forms. The thus derived differential profile of the antiradical capacity of all vanadium compound forms may reflect, among others, the influence of the oxidation state of V(V) or V(IV) or V(IV,V) in bound DPOT, in the encapsulated form, on the %RSC. Although all vanadium compounds used in this work exhibited similar radical scavenging patterns, the SiO_2-encapsulated vanadium forms exhibited enhanced RSC properties compared to their free forms. This enhancement may imply enhanced bioavailability, protected bioactivity, and targeted controlled release of

vanadium from their nanohosts, on site, during their 24 h incubation period in the microorganism environment.

Collectively, both ROS scavenging activity and free radical scavenging capacity results on both cell lines, suggest that a) the encapsulated forms of vanadium appear to deliver more potent antioxidant activity than their non-encapsulated counter parts; b) albeit of different methodologies employed in the assays for the determination of ROS species, the results of one methodology do not contradict the other, thereby lending credence to the complementarity of the results obtained in the formulation of the antioxidant profile of vanadium compounds containing the discrete or mixed oxidation states of vanadium; and c) the observed antioxidant behavior appears to be concentration-dependent, thereby signifying the importance of concentration in the efficient neutralization of ROS species of varying nature.

5. Conclusions

For the first time, free radical and reactive oxygen species scavenging properties of well-defined V(IV), V(V), and V(IV,V) vanadium compounds were examined in comparison to their encapsulated vanadium-loaded counterparts in SiO_2 NPs. For that reason, the synthesis of a heterometallic lithium-bearing tetranuclear assembly of V(IV,V) dimers bound to the suitable chelator $[DPOT]^{5-}$ and their sol-gel encapsulation compounds in SiO_2 NPs were also successfully pursued. The results laid the grounds for the development of efficient antioxidant and antiradical vanadium nanomaterials. The vanadium oxidation state a) embedded in a well-configured and defined metal-bound organic substrate structure, such as that of VDPOT, and b) combined with the process of encapsulation, suggests that appropriately formulated structural motifs of vanadium complex assemblies merit further research into the maintenance of homeostatic processes linked to the antioxidant status of cells. That type of hybrid (nano)materials may improve therapeutic potency, enhance protection against degradation, optimization in pharmacokinetics, promote better control of biodistribution, and decrease cytotoxicity, consistent with a controlled, targeted, localized and steady vanadium release rate against oxidative stress and free radical activity.

Abbreviation list

DPPH	2-diphenyl-1-picrylhydrazyl
ROS	reactive oxygen species
NP(s)	nanoparticle(s)
DPOT	1,3-diamine-2-propanol-*N*,*N*,*N*′,*N*′-tetraacetic acid
FT-IR	Fourier–transform infrared spectroscopy
ESI-MS	electrospray ionization-mass spectrometry
UV–Vis	Ultraviolet–Visible
RSC	Radical Scavenging Capacity
TGA	thermogravimetric analysis
XRD	X-ray diffraction
SEM	scanning electron microscopy
BET	Brunauer–Emmett–Teller
BJH	Barrett-Joyner-Halenda
PSD	pore size distribution
NMR	nuclear magnetic resonance
MAS	magic angle spinning
CP	cross polarization
SD	Standard deviation
PMS-NADH	phenazine methosulfate-NADH
NBT	nitroblue tetrazolium
BS	*Bacillus subtilis*
EC	*Escherichia coli*
MMS	Minimal Mineral Salts
OD	optical density
CFU	colony-forming unit
TEOS	tetraethoxysilane
BBB	blood brain barrier

Appendix A. Supplementary data

CCDC 1508538 (**1**) contains the supplementary crystallographic data for this paper. These data can be obtained free of charge via www.ccdc.cam.ac.uk/data_request/cif, or by emailing data_request@ccdc.cam.ac.uk, or by contacting The Cambridge Crystallographic Data Centre, 12 Union Road, Cambridge CB2 1EZ, UK; fax: +44 1223 336033. Supplementary data associated with this article can be found in the online version, at https://doi.org/10.1016/j.jinorgbio.2018.12.005.

References

[1] N.D. Chasteen, Met. Ions Biol. Syst. 31 (1995) 231–247.
[2] H. Boukhalfa, A.L. Crumbliss, Biometals 15 (2002) 325–339.
[3] A.S. Cornish, W.J. Page, Appl. Environ. Microbiol. 66 (2000) 1580–1586.
[4] E.J. Baran, J. Inorg. Biochem. 80 (2000) 1–10.
[5] E.G. Ferrer, P.A.M. Williams, E.J. Baran, Biol. Trace Elem. Res. 105 (2005) 53–58.
[6] P.A.M. Williams, S.B. Etcheverry, D.A. Barrio, E.J. Baran, Carbohydr. Res. 341 (2006) 717–724.
[7] U. Jungwirth, C.R. Kowol, B.K. Keppler, C.G. Hartinger, W. Berger, P. Heffeter, Antioxid. Redox Signal. 15 (2011) 1085–1127.
[8] I.G. Macara, K. Kustin, L.C. Cantley, Biochim. Biophys. Acta 629 (1980) 95–106.
[9] R. Francik, M. Krośniak, M. Barlik, A. Kudła, R. Grybos, T. Librowski, Bioinorg. Chem. Appl. 2011 (2011) 206316.
[10] L. Packer, Diabetologia 36 (1993) 1212–1213.
[11] B. Łacka, W. Grzeszczak, Pol. Arch. Med. Wewn. 98 (1997) 67–75.
[12] I. Zwolak, H. Zaporowska, Acta Biol. Hung. 60 (2009) 55–67.
[13] B. Halliwell, Annu. Rev. Nutr. 16 (1996) 33–50.
[14] O.I. Aruoma, J. Am. Oil Chem. Soc. 75 (1998) 199–212.
[15] N. Balasundram, K. Sundram, S. Samman, Food Chem. 99 (2006) 191–203.
[16] S. Al-Malaika, G. Pritchard (Ed.), Plastic Additives, Chapman and Hall, London, 1998, p. 56.
[17] K.C. Waterman, R.C. Adami, K.M. Alsante, J. Hong, M.S. Landis, F. Lombardo, C.J. Roberts, Pharm. Dev. Technol. 7 (2002) 1–32.
[18] Y. Deligiannakis, G.A. Sotiriou, S.E. Pratsinis, ACS Appl. Mater. Interfaces 4 (2012) 6609–6617.
[19] R.J. Debus, Biochim. Biophys. Acta 1102 (1992) 269–352.
[20] R.W. Rex, Nature 188 (1960) 1185–1186.
[21] S.E. Pratsinis, D.S. Ensor, K.N. Lohr (Eds.), History of Manufacture of Fine Particles in High Temperature Aerosol Reactors, RTI Press, Research Triangle Park, NC, 2011, pp. 475–507 (Chapter 18).
[22] M. Vallet-Regi, F. Balas, D. Arcos, Angew. Chem. Int. Ed. 46 (2007) 7548–7558.
[23] T.J. Brunner, P. Wick, P. Manser, P. Spohn, R.N. Grass, L.K. Limbach, A. Bruinink, W.J. Stark, Environ. Sci. Technol. 40 (2006) 4374–4381.
[24] a) K. Kanamori, K. Nishida, N. Miyata, T. Shimoyama, K. Hata, C. Mihara, K. Okamoto, Y. Abe, S. Hayakawa, S. Matsugo, Inorg. Chem. 43 (2004) 7127–7140; b) H. Kumagai, S. Kawata, S. Kitagawa, K. Kanamori, K. Okamoto, Chem. Lett. (1997) 249–250.
[25] Rigaku/MSC, CrystalClear, Rigaku/MSC Inc., The Woodlands, Texas, USA, 2005.
[26] G.M. Sheldrick, Acta Cryst A64 (2008) 112–122.
[27] S. Nagappan, C.S. Ha, J. Coat. Sci. Technol. 1 (2014) 151–160.
[28] A. Kagiava, A. Tsingotjidou, C. Emmanouilides, G. Theophilidis, Neurotoxicology (2008) 1100–1106.
[29] W.R. Biggs, R.J. Brown, J.C. Fetzer, Energy Fuel 1 (1987) 257–262.
[30] M.C. Becerra, A.J. Eraso, I. Albesa, Luminescence 18 (2003) 334–340.
[31] M. Özyürek, D. Akpinar, M. Bener, B. Türkkan, K. Güçlü, R. Apak, Chem. Biol. Interact. 212 (2014) 40–46.
[32] M. Cavia-Saiz, M.D. Busto, M.C. Pilar-Izquierdo, N. Ortega, M. Perez-Mateos, P. Muñiz, J. Sci. Food Agric. 90 (2010) 1238–1244.
[33] W. Brand-Williams, M.E. Cuvelier, C. Berset, LWT- Food Sci. Technol. 28 (1995) 25–30.
[34] K. Mishra, H. Ojha, N.K. Chaudhury, Food Chem. 130 (2012) 1036–1043.
[35] C. Sanchez-Moreno, Food Sci. Technol. Int. 8 (2002) 121–137.
[36] V.B. Kandimalla, V.S. Tripathi, H. Ju, Crit. Rev. Anal. Chem. 36 (2006) 73–106.
[37] D. Peak, R.G. Ford, D.L. Sparks, J. Colloid Interface Sci. 218 (1999) 289–299.
[38] M.D. Wildberger, T. Mallat, U. Göbel, A. Baiker, Appl. Catal. A Gen. 168 (1998) 69–80.
[39] G. Bellussi, M.S. Rigutto, Stud. Surf. Sci. Catal. 85 (1994) 177–203.
[40] D.C.M. Dutoit, M. Schneider, P. Fabrizioli, A. Baiker, J. Mater. Chem. 7 (1997) 271–278.
[41] M. Baltes, K. Cassiers, P. Van Der Voort, B.M. Weckhuysen, R.A. Schoonheydt, E.F. Vansant, J. Catal. 197 (2001) 160–171.
[42] V. Murgia, E.M. Farfán Torres, J.C. Gottifredi, E.L. Sham, Appl. Catal. A Gen. 312 (2006) 134–143.
[43] R.M. Almeida, T.A. Guiton, C.G. Pantano, J. Non-Cryst. Solids 121 (1990) 193–197.
[44] J. Gallardo, A. Durán, D. Di Martino, R.M. Almeida, J. Non-Cryst. Solids 298 (2002) 219–225.
[45] P. Innocenzi, J. Non-Cryst. Solids 316 (2003) 309–319.
[46] M. Cerruti, G. Magnacca, V. Bolis, C. Morterra, J. Mater. Chem. 13 (2003) 1279–1286.
[47] N.J. Clayden, S. Esposito, P. Pernice, A. Aronne, J. Mater. Chem. 12 (2002)

3746–3753.
[48] I. Correia, J.C. Pessoa, M.T. Duarte, M.F. Minas da Piedade, T. Jackush, T. Kiss, M.M.C.A. Castro, C.F.G.C. Geraldes, F. Avecilla, Eur. J. Inorg. Chem. (2005) 732–744.
[49] D.F. Evans, P.H. Missen, J. Chem. Soc. Dalton Trans. (1987) 1279–1281.
[50] a) M. Matzapetakis, C.P. Raptopoulou, A. Terzis, A. Lakatos, T. Kiss, A. Salifoglou, Inorg. Chem. 38 (1999) 618–619;
b) M. Matzapetakis, C.P. Raptopoulou, A. Tsohos, B. Papefthymiou, N. Moon, A. Salifoglou, J. Am. Chem. Soc. 120 (1998) 13266–13267;
c) M. Matzapetakis, M. Dakanali, C.P. Raptopoulou, V. Tangoulis, A. Terzis, N. Moon, J. Giapintzakis, A. Salifoglou, J. Biol. Inorg. Chem. 5 (2000) 469–474;
d) M. Matzapetakis, N. Karligiano, A. Bino, M. Dakanali, C.P. Raptopoulou, V. Tangoulis, A. Terzis, J. Giapintzakis, A. Salifoglou, Inorg. Chem. 39 (2000) 4044–4051;
e) M. Matzapetakis, M. Kourgiantakis, M. Dakanali, C.P. Raptopoulou, A. Terzis, A. Lakatos, T. Kiss, I. Banyai, L. Iordanidis, T. Mavromoustakos, A. Salifoglou, Inorg. Chem. 40 (2001) 1734–1744.
[51] a) C. Gabriel, J. Venetis, M. Kaliva, C.P. Raptopoulou, A. Terzis, C. Drouza, B. Meier, G. Voyiatzis, C. Potamitis, A. Salifoglou, J. Inorg. Biochem. 103 (2009) 503–516;
b) M. Tsaramyrsi, M. Kaliva, C.P. Raptopoulou, A. Terzis, V. Tangoulis, J. Giapintzakis, A. Salifoglou, Inorg. Chem. 40 (2001) 5772–5779;
c) M. Kaliva, C. Gabriel, C.P. Raptopoulou, A. Terzis, G. Voyiatzis, M. Zervou, C. Mateescu, A. Salifoglou, Inorg. Chem. 50 (2011) 11423–11436.
[52] E. Halevas, E. Chatzigeorgiou, S. Hadjispyrou, A. Hatzidimitriou, V. Psycharis, A. Salifoglou, Polyhedron 127 (2017) 420–431.
[53] E. Halevas, A. Hatzidimitriou, C. Gabriel, C. Mateescu, A. Salifoglou, Inorg. Chim. Acta 453 (2016) 667–680.
[54] C. Duval, Inorganic Thermogravimetric Analysis, Second and Revised edition, Elsevier Publishing Co., Amsterdam, 1963.
[55] V. Sacchetto, G. Gatti, G. Paul, I. Braschi, G. Berlier, M. Cossi, L. Marchese, R. Bagatin, C. Bisio, Phys. Chem. Chem. Phys. 15 (2013) 13275–13287.
[56] R.F. De Farias, C. Airoldi, J. Therm. Anal. 53 (1998) 751–756.
[57] S. Esposito, M. Turco, G. Ramis, G. Bagnasco, P. Pernice, C. Pagliuca, M. Bevilacqua, A. Aronne, J. Solid State Chem. 180 (2007) 3341–3350.
[58] J. Roch, Compt. Rend. 248 (1959) 3549–3551.
[59] X. Guo, N. Xue, S. Liu, X. Guo, W. Ding, W. Hou, Microporous Mesoporous Mater. 106 (2007) 246–255.
[60] G.S. Pappas, P. Liatsi, I.A. Kartsonakis, I. Danilidis, G. Kordas, J. Non-Cryst. Solids 354 (2008) 755–760.
[61] IUPAC Recommendations, Pure Appl. Chem. 57 (1985) 603–609.
[62] X. Du, J. He, J. Colloid Interface Sci. 345 (2010) 269–277.
[63] C.J. Brinker, G.W. Scherer, Sol-Gel Science - The Physics and Chemistry of Sol-Gel Processing, Academic Press, New York, 1990.
[64] H. Dislich, J. Non-Cryst. Solids 73 (1985) 599–612.
[65] H. Dislich, J. Non-Cryst. Solids 80 (1986) 115–121.
[66] E. Halevas, C.M. Nday, E. Kaprara, V. Psycharis, C.P. Raptopoulou, G.E. Jackson, G. Litsardakis, A. Salifoglou, J. Inorg. Biochem. 151 (2015) 150–163.
[67] D.E. Keller, T. Visser, F. Soulimani, D.C. Koningsberger, M.B. Weckhuysen, Vib. Spectrosc. 43 (2007) 140–151.
[68] M. Mathieu, P. Van Der Voort, B.M. Weckhuysen, R.R. Rao, G. Catana, R.A. Schoonheydt, E.F. Vansant, J. Phys. Chem. B 105 (2001) 3393–3399.
[69] R. Bulanek, L. Capek, M. Setnicka, P. Cicmanec, J. Phys. Chem. C 115 (2011) 12430–12438.
[70] B. Solsona, T. Blasco, J.M.L. Nieto, M.L. Pena, F. Rey, A. Vidal-Moya, J. Catal. 203 (2001) 443–452.
[71] A.K. Rahiman, K.S. Bharathi, S. Sreedaran, K. Rajesh, V. Narayanan, Inorg. Chim. Acta 362 (2009) 1810–1818.
[72] J.C. Robles, Y. Matsuzaka, S. Inomata, M. Shimoi, W. Mori, H. Ogino, Inorg. Chem. 32 (1993) 13–17.
[73] J.C. Robles, M. Shimoi, H. Ogino, Chem. Lett. 21 (1992) 309–310.
[74] P. Trumbo, A.A. Yates, S. Schlicker, M. Poos, J. Am. Diet. Assoc. 101 (2001) 294–301.
[75] R.S. Soumya, R. Reshmi, S. Jomon, K.A. Antu, M.P. Riya, K.G. Raghu, Food Funct. 5 (2014) 535–544.
[76] L.A. Soriano-Agueda, C. Ortega-Moo, J. Garza, J.A. Guevara-García, R. Vargas, Comput. Theor. Chem. 1077 (2016) 99–105.
[77] G. Scalese, I. Correia, J. Benítez, S. Rostán, F. Marques, F. Mendes, A.P. Matos, J.C. Pessoa, D. Gambino, J. Inorg. Biochem. 166 (2017) 162–172.
[78] A. Staško, V. Brezová, S. Biskupič, V. Mišík, Free Radic. Res. 41 (4) (2007) 379–390.